

## CONTENTS

	<b>Page</b>
Apparatus for Density and Dielectric Constant Measurements to 35 MPa on Fluids of Cryogenic Interest – W. M. Haynes and N. V. Frederick .....	241
An Intercomparison of Pressure Standards Between the Istituto di Metrologia “G. Colonnetti” and the National Bureau of Standards – J.C. Houck, G. F. Molinar, and R. Maghenzani .....	253
Analysis of Liquid Flow-Induced Motion of a Discrete Solid in a Partially Filled Pipe – Bal M. Mahajan .....	261
List of Publications of the National Bureau of Standards .....	289

Library of Congress Catalog Card Number: 63-37059

---

For sale by the Superintendent of Documents, U.S. Government Printing Office  
Washington, DC 20402

Single copy price \$5.50 Domestic; \$6.90 Foreign.

Subscription price: \$18.00 a year; \$22.50 foreign mailing.

UNITED STATES GOVERNMENT PRINTING OFFICE, WASHINGTON: 1983

# Apparatus for Density and Dielectric Constant Measurements to 35 MPa on Fluids of Cryogenic Interest

W. M. Haynes and N. V. Frederick  
National Bureau of Standards, Boulder, CO 80303

Accepted: March 11, 1983

An apparatus has been developed for simultaneous measurements of fluid densities and dielectric constants at temperatures from 70 to 320 K and at pressures to 35 MPa. A magnetic suspension technique, based on an application of Archimedes' principle, is employed in the density determination, while a concentric cylinder capacitor is used for obtaining the dielectric constant data. The apparatus can be used not only for determining densities and dielectric constants of compressed gases and liquids (including mixtures), but for saturated liquid and vapor properties as well. Also included is the capability for acquiring liquid-vapor equilibrium data for mixtures. The total uncertainty of a single density measurement is estimated to be approximately 0.1% for densities as low as 50 kg/m<sup>3</sup>; at lower densities, the uncertainty increases. The imprecision of the density data is typically less than 0.02%. The total uncertainty in the dielectric constants is approximately 0.01%. Experimental data for a 0.85 CH<sub>4</sub>+0.15 C<sub>2</sub>H<sub>6</sub> mixture are given here to demonstrate the performance of the apparatus.

Key words: Clausius-Mossotti function; compressed fluid; concentric cylinder capacitor; density; dielectric constant; excess volume; magnetic suspension densimeter; methane-ethane mixture; saturated liquid; vapor pressure.

## 1. Introduction

A magnetic suspension densimeter [1,2]<sup>1</sup> was used in a large-scale program to measure the orthobaric liquid densities of the major components [1,3,4] of liquefied natural gas (LNG) and mixtures [5-9] of these components. This technique, based on an application of Archimedes' principle, was selected for the LNG density project for several reasons:

- 1) It is capable of absolute density measurements of high accuracy and precision over wide ranges of

**About the Authors, Paper:** W. M. Haynes is with NBS' Chemical Engineering Science Division, and N. V. Frederick with its Electromagnetic Technology Division. The work reported on was carried out at NBS under the sponsorship of the American Gas Association, Inc. and the National Aeronautics and Space Administration.

<sup>1</sup> Figures in brackets indicate literature references at the end of this paper.

- density, temperature, and pressure.
- 2) Calibration fluids are not required.
- 3) The technique can be used not only to measure densities of compressed fluids, but also to measure liquid and vapor densities along the coexistence boundary.

The measurements for the LNG density project were concentrated in the temperature range from 100-140 K at pressures typically less than 0.2 MPa. The apparatus was designed for a maximum pressure of 5 MPa. Near the end of the LNG density project, the pressure range of the densimeter was expanded to at least 35 MPa. The expansion was because of a need to map the PVT surfaces of fluids with critical points significantly above ambient temperature. (A gas expansion technique [10-13] used at this laboratory for PVT measurements on cryogenic fluids could not be used for this application.) The expansion of the densimeter's pressure capability resulted in a new instrument, described here, significantly different from and more versatile than the previous one [1] developed specifically for the LNG density project.

Although many of the components of the new densimeter changed, the technique used is the same. To detect the position of the magnetic buoy, a linear differential capacitance sensor [12], compatible with the higher pressure environment, has been developed to replace an inductance sensor. Although the properties of the buoy had been well characterized in the previous work [1], it was necessary to determine the effect of pressure on its volume. A new support coil for lifting the buoy and a new microscope lens combination for determining the position of the buoy were also required in adapting the technique to higher pressures.

Since the dielectric constant of a fluid is closely related to its density through the Clausius-Mossotti function, a concentric cylinder capacitor was added inside the sample cell to enable simultaneous measurements of dielectric constant and density on the same fluid samples. Dielectric constant measurements can serve as simple and reliable substitutes for density measurements. The addition of the capacitor was motivated to some extent by the fact that some commercial densimeters being developed for custody transfer applications in LNG transactions include devices based on capacitance measurements.

The new apparatus incorporates a cryostat design different from that employed with the previous densimeter, but similar to ones used with other instruments [10–13] in this laboratory. The cryostat is suitable for continuous temperature control between 70 and 320 K. A new high-pressure window design developed for the equilibrium cell allows the position of the buoy to be determined by optical means. With the new cell and cryostat, it was not possible to change the position of the buoy by mechanical means; this is now accomplished electronically.

The apparatus can also be used for liquid-vapor equilibrium measurements on mixtures. Means have been provided for mixing (recirculation of vapor through liquid), sampling of vapor and liquid, and subsequent composition analysis. Compared to the previous densimeter [1], improvements have been made in the characterization of the temperature, pressure, and composition of the fluid samples. With the previous apparatus [1], it was possible to observe the liquid-vapor interface through a window that extended most of the length of the sample space. In adapting the magnetic suspension densimeter for pressures to 35 MPa over a wide temperature range, it was not practical to retain this feature. This feature, although convenient, was not essential for any of the measurements performed with the new apparatus.

The new apparatus was first used to complete

measurements for the LNG density project [7,9]. Extensive tests were made to ensure that the density results obtained with the new apparatus were in agreement with those from the previous apparatus. The consistency of the density data was one of the most important considerations in the development of mathematical models [15–18] for predictions of mixture (LNG) densities. The apparatus was then used to measure the densities and dielectric constants of liquid propane [19–20], isobutane [19,21], and normal butane [19,22] over temperature ranges from their triple points to 300 K at pressures to 35 MPa.

## 2. Measurement Methods

### 2.1 Density

In the magnetic suspension densimeter used, a piece of magnetic material (barium ferrite magnetic buoy in the shape of a right circular cylinder magnetized along its cylindrical axis) is suspended freely by the force produced from the axial magnetic field of a single air-core solenoid. The vertical motion of the magnetic buoy is controlled by the automatic regulation of the solenoid current with a closed-loop servocircuit that includes a differential capacitance sensor to detect the position of the buoy. (The horizontal position of the buoy is maintained by the axially symmetrical, diverging field of the solenoid.) In the present system, the magnetic buoy is more dense than the fluids in which it is suspended. Thus, an upward magnetic force is added to the buoyant force to balance the downward gravitational force.

In earlier work [2] with a densimeter that utilized a three-solenoid arrangement to supply the magnetic force, it was found that the magnetic moment of a barium ferrite buoy was independent of magnetic field intensity over the range of fields (0.006–0.016 T) needed to support the buoy. Barium ferrite is a magnetically hard material with a permanent moment. This meant that a one-coil system could be used to determine fluid densities without the need of calibration fluids. To carry out density measurements with a one-coil system and a barium ferrite buoy, first the current ( $I_v$ ) necessary to support the buoy in vacuum at a given position (buoy-coil separation distance) and temperature is measured. Then the current ( $I_f$ ) necessary to support the buoy in a fluid of unknown density at the same position and temperature is determined. The density ( $\rho$ ) of the fluid is related to these currents by the relation,

$$\rho = \frac{m}{V} \left( 1 - \frac{I_f}{I_v} \right), \quad (1)$$

where  $m$  and  $V$  are the mass and volume of the buoy. Measurement procedures for using this equation to determine fluid densities for the instrument developed in the present work are discussed later. Also presented is a detailed description of the magnetic suspension system.

## 2.2 Dielectric Constant

A stable concentric cylinder capacitor was used for dielectric constant measurements. First, the capacitance ( $C$ ) with the fluid (of unknown dielectric constant) between the cylindrical electrodes is measured. Then, at the same temperature, the vacuum capacitance ( $C_0$ ) is determined. The dielectric constant ( $\epsilon$ ) is calculated from the relation,

$$\epsilon = C/C_0. \quad (2)$$

## 3. Apparatus

### 3.1 Cryostat

The major features of the cryostat are shown to scale in figure 1, an assembly drawing of the apparatus. This cryostat is similar to some used previously at this laboratory [10–13]. Those modifications necessary to adapt the cryostat for use with a magnetic suspension densimeter will be emphasized.

The cryostat was supported by a 1.3-cm-thick aluminum plate suspended from concrete block columns at a height 2.3 m above floor level. The aluminum plate was reinforced with 10-cm-wide stainless steel channel beams so that the position of the cryostat was independent of the amount of liquid nitrogen in the reservoir. Apparent changes in the buoy-coil separation distance resulted if the position of the cryostat was not maintained during the course of measurements. The aluminum plate from which the cryostat was suspended could be leveled and clamped in place using four bolts in contact with the concrete block columns.

The cryostat was fabricated from nonmagnetic materials. The inner cylinders or cans (liquid nitrogen reservoir, cold ring, guard ring, shield, cold wall) were copper; the outer vacuum jacket and access tubes were primarily stainless steel; and the flanges, support plates, and fittings were mostly brass. The various cylindrical portions of the cryostat and the central support (reflux) tube had to be aligned (concentric and vertical) so the buoy could be suspended symmetrically about the cylindrical axis of the differential capacitance sensor. Many of the dimensions of the cryostat components were

determined by the dimensions of the high-pressure cell and the support coil. The outside diameter of the stainless steel vacuum jacket is 20.3 cm while the outside diameter of the glass tail of the cryostat is 9.0 cm. There is 0.4-cm clearance on the diameter between the cryostat tail and the support coil. The

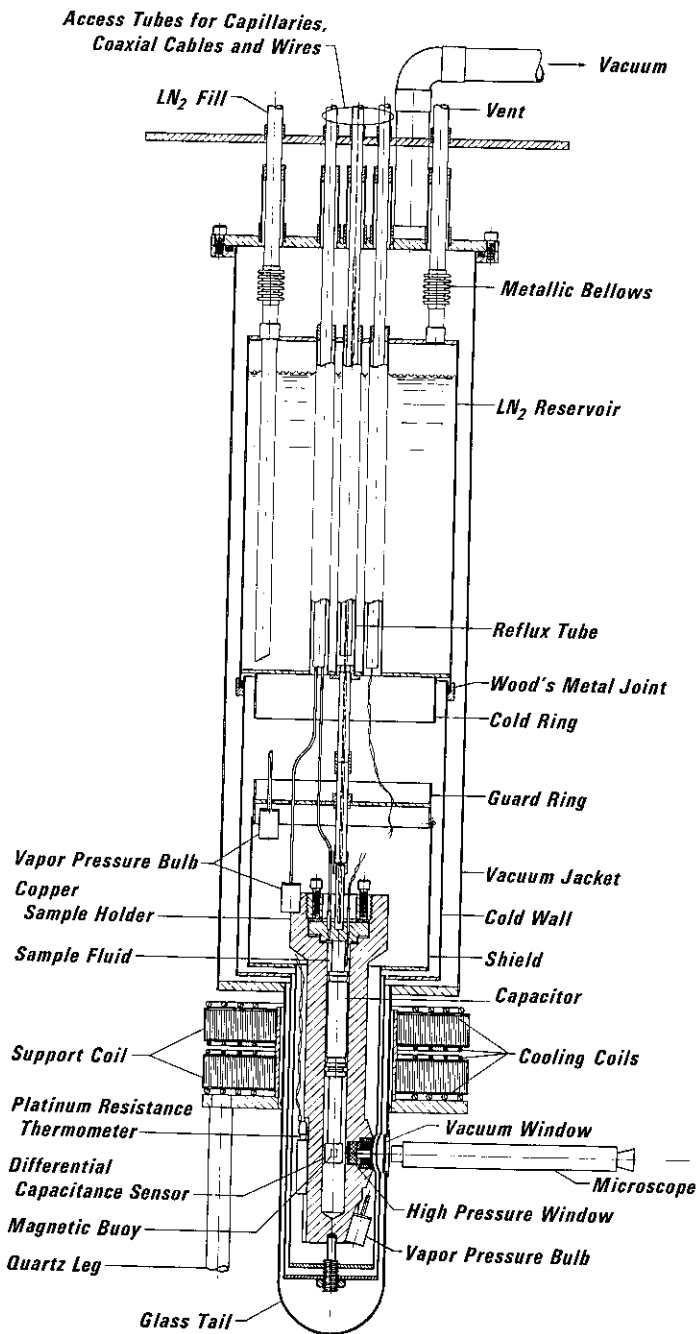


Figure 1—Assembly drawing (approximately to scale) of an apparatus for density and dielectric constant measurements to 35 MPa on cryogenic fluids.

overall length of the cryostat is approximately 94 cm.

The liquid nitrogen reservoir has a capacity of approximately  $7 \times 10^3 \text{ cm}^3$  and needs refilling under normal conditions about every 16 h. Metallic bellows were placed in the fill and vent lines of the reservoir to eliminate relative movement, as a function of temperature, between the cell and the outer stainless steel jacket of the cryostat. This step was necessary to maintain alignment of the capacitance sensor and buoy located inside the cell with the support coil located outside the cryostat, independent of the experimental conditions. Five access tubes, which passed through the liquid nitrogen reservoir, were available for introducing capillaries, coaxial cables, and wires into the vacuum space and cell inside the cryostat.

The cryostat was comprised of one large vacuum space; holes (3 cm diameter) were cut into the electroformed copper cylinders attached to the liquid nitrogen reservoir and the guard ring for visual observation of the buoy. With this arrangement it was not feasible to use exchange gas for fast-cooling the cell. The exchange gas would have been in direct contact with the outer stainless steel can which included a glass tail as its lower section. The glass tail was connected to the outer jacket through a stainless steel-to-glass transition joint; to ensure integrity of this seal, the joint should be kept at a temperature near ambient.

Fast-cooling of the cell was accomplished using the refluxing action of nitrogen in the central support tube. The maximum cooling rate was approximately 50 K/h. The reflux tube is evacuated during measurements when the cell is controlled at a desired temperature. For additional cooling, three flexible copper braided straps (not shown in fig. 1), each with a cross sectional area of  $5 \text{ mm}^2$  per strap, have been connected symmetrically from the top of the cold shield to the cell.

The cryostat was designed to facilitate ease in assembly and disassembly and to minimize alignment problems of critical components. All demountable joints had enough latitude to make alignment reasonably straightforward. The outer vacuum jacket was attached to the top of the cryostat through a rubber o-ring seal using a split-ring assembly not shown in the drawing. The inner cans were attached with either Wood's metal or screws. Once the joints were secured, the entire structure was rigid, and no problems with alignment were encountered after numerous temperature cycles. A nut and bolt (fiberglass) arrangement was installed between the cold shield and the bottom of the cell to eliminate pendulous vibrations of the cell.

### 3.2 Equilibrium Sample Cell

Figure 2 is a detailed cross sectional diagram of the copper equilibrium cell. The overall dimensions of the cell used here are roughly the same as for the cell used with the earlier version [1] of the magnetic suspension densimeter, except for an increase in the wall thickness required for use at higher pressures. The new cell has an overall length of approximately 29.5 cm, primarily determined by the position at which the buoy must be suspended relative to the diverging field of the support coil for horizontal stability of the buoy. The outside diameter of the main part of the cell is 4.44 cm, while

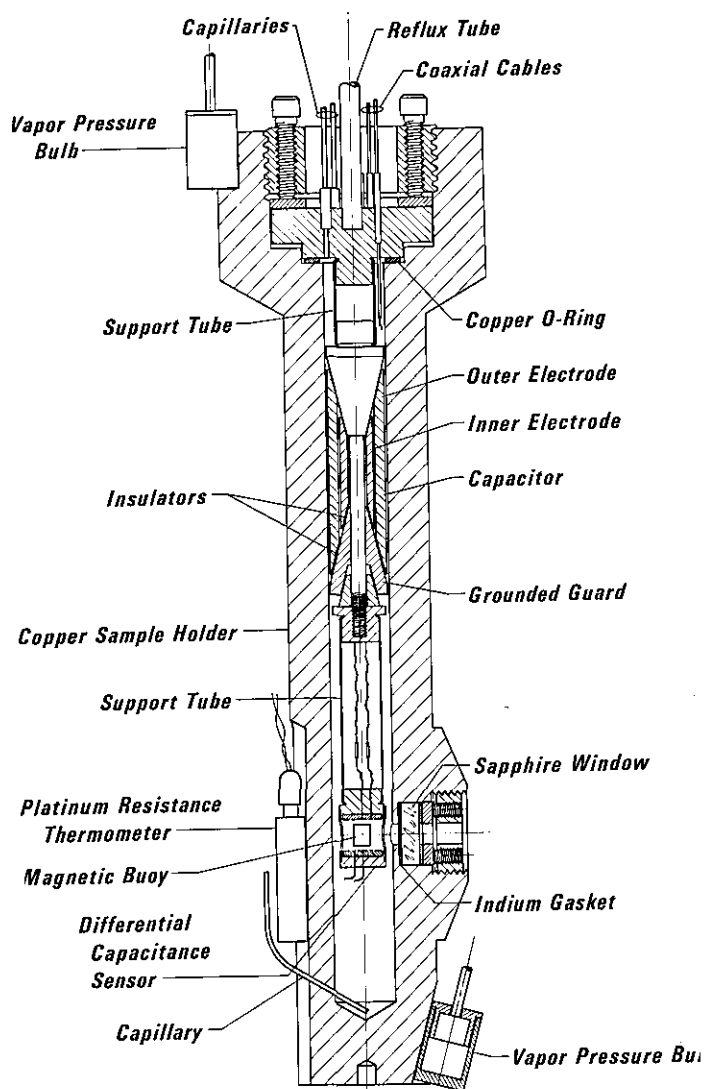


Figure 2—The equilibrium cell.

the top closure section has a diameter of 8.10 cm. The dimensions of the internal sample space are 1.90 cm diameter by approximately 23 cm length. About one third of the internal volume is occupied by the concentric cylinder capacitor and the magnetic buoy-capacitance sensor assembly. This results in an internal free volume of approximately 43 cm<sup>3</sup>, as determined by filling the cell with water.

To facilitate easy access to the assemblies inside the cell, a flange-gasketed seal was used to close the cell. The seal was effected by compressing a silver-plated, solid copper O-ring between a stainless steel plug and a smooth, flat ledge of the copper cell. This assembly was similar to that used earlier [1]. A thin-walled stainless steel tube, used to support the cell, was soldered into the cell lid (the stainless steel closure plug). This support tube was also used for reflux gas as described earlier.

For visual observation of the magnetic buoy position, a new window assembly for pressures to 35 MPa has been developed. The assembly consists of a sapphire disk (1.90 cm diameter by 0.63 cm thickness) with chamfered edges, indium gasket, asbestos-rubber backing ring to relieve thermal and mechanical strains, and stainless steel plug and ring with four stainless steel set screws to provide a pressure- and vacuum-tight seal. It has a 0.63 cm diameter viewing area. An effort was made to minimize the size of the high pressure window assembly, especially in the horizontal direction. This effort resulted from an attempt to minimize the inner diameter of the support coil so current and power in the coil were not excessively large.

A total of four capillaries has been introduced into the sample space. Two capillaries are soldered into collars in the cell lid; the other two are soldered into the cell wall with their ends terminating at the bottom of the sample space. This makes it possible to fill the cell from either the top or bottom, or from both simultaneously. Filling procedures can be critical when condensing liquid mixtures into the cell. Under normal conditions, a pair of capillaries, one at the top and one at the bottom, is available for recirculating the vapor through the liquid for mixing; the other capillary at the top is for pressure measurements while the free capillary at the bottom can be used for liquid sampling. By having capillaries at both ends of the cell, it is easy to remove low vapor pressure liquids from the cell.

At approximately the same height at which the magnetic buoy is suspended, a platinum resistance thermometer has been soldered with indium into a closed-end copper tube that has been soft-soldered into

a groove cut lengthwise in the cell wall. Vapor pressure bulbs fabricated from copper (each with an internal volume of approximately 2 cm<sup>3</sup>) have been installed at the ends of the cell in close thermal contact (soft-solder) with the outside surface. These bulbs, along with differential thermocouples (chromel-constantan) secured at the same positions, are used to monitor temperature differences between the ends of the cell. Four independent heaters of 110 to 160  $\Omega$  each for temperature control have been wound bifilarly at different positions along the length of the cell.

A total of six coaxial cables enter through the lid of the cell into the sample space in pressure-tight assemblies. Three of the cables are for the capacitance sensor, two for the cylindrical capacitor, and one is a spare. Each coaxial cable consists of an outer stainless steel sheath of 0.51 mm diameter insulated from a 0.13 mm diameter inner conductor with polytetrafluoroethylene. These cables have been found to be leak-tight along short lengths at gas pressures to 70 MPa at room temperature. Cables approximately 1 meter in length have been inserted into stainless steel capillaries (1.07 mm outside diameter  $\times$  0.66 mm inside diameter) that extend from inside the sample cell to a position above the top of the cryostat where the coaxial cables are soldered into the capillaries. This means that continuous lengths of the coaxial cables extend from inside the sample cell to a region in which the cables are leak-tight. At low temperatures, the cables do not seal because of the relatively large difference in the thermal expansion coefficients of stainless steel and polytetrafluoroethylene. The stainless steel capillaries are soldered into collars in the lid of the cell and at the top of the cryostat.

### 3.3 Magnetic Suspension System

The magnetic suspension system, employed here in the density determination, uses some components from the previous densimeter [1]. The magnetic buoy, with its well-characterized properties deduced from the earlier work, has been described in detail. The buoy is a barium ferrite magnet in the shape of a right circular cylinder (0.51 cm diameter  $\times$  0.64 cm length) magnetized along its cylindrical axis. Barium ferrite is a magnetically hard, ceramic material with a density of approximately  $5 \times 10^3$  kg/m<sup>3</sup>. Since barium ferrite is porous, the buoy was plated with copper to a thickness of approximately 0.06 mm. A thin ( $10^{-3}$  mm) protective coating of gold was flashed over the copper. No problems were encountered with fluids penetrating the copper layer at pressures to 35 MPa.

Barium ferrite was selected as the buoy material since its magnetic properties are consistent with absolute density measurements [2]. Over the range of magnetic fields needed to support the buoy, the magnetic moment of the barium ferrite buoy had been found to be independent of the magnetic field intensity.

The densimeter described here included a single solenoid that supplied the force required to lift the buoy. The simplification in the densimeter design in going from a three-coil to a one-coil system, which resulted from a determination of the magnetic properties of barium ferrite, has been discussed in detail in an earlier paper [2]. (Although no further use of a three-coil arrangement with gradient coils was anticipated, the outside diameter of the new support coil was made less than the inside diameter of the gradient coils used in the previous work [1] in the eventuality that a need for tests on new buoy materials ensued.)

The new support coil is composed of two separate coils of 2275 turns each of epoxy-coated aluminum foil of approximately 0.025 mm thickness and 2.5 cm width. Each of the two coils, epoxied to a central quartz tube at a separation distance of 1.3 cm, has an inside diameter of 10.16 cm and an outside diameter of roughly 22.2 cm. To be compatible with the new higher-pressure cell, the inside diameter of the new coil is somewhat larger than that used previously [1]. The quartz tube is attached to a fiberglass plate supported by three quartz rods (2.54 cm diameter) that extend to another fiberglass plate resting on a part of the concrete block structure, used for rigid support of the entire apparatus. Water-cooled copper plates, insulated with thin mylar sheets, have been placed in close thermal contact with all faces of the two coils. No problems have been encountered with this arrangement for mounting and cooling the coils for use at currents to 1.5 A, which corresponds to 270 W heat dissipation in the coils.

The servocircuit is essentially the same as that used before [1] except for a new type of sensor for detecting the position of the buoy. Some problems had been encountered with the earlier densimeter [1] with pressurized fluid slowly penetrating into the coil windings of an inductance sensor, resulting in a slow change in the position of the suspended buoy. Thus, a differential capacitance sensor [13], a solid monolithic structure, has been developed for position detection in the present work that entails measurements in fluids at pressures to 35 MPa. The sensitivity of the capacitance sensor was at least equivalent to that of the linear differential transformer used previously. By balancing a bridge of which the sensor is a part, the

position of the buoy can be made insensitive to the dielectric constant of the sample fluid. For a detailed description of the capacitance sensor, see reference [13].

The previous densimeter [1] included mechanical means for fine adjustment of the position of the buoy in going from vacuum-to-liquid measurements. The new system does not incorporate this feature. Small changes in the buoy position are accomplished electronically in the new system by adjusting the offset voltage of the integrator amplifier in the servocircuit. A calibrated 0.5- $\Omega$  standard resistor, placed in series with the support coil, can handle the relatively large currents needed to lift the buoy in the present work. The measurement of the voltage drop across this resistor, which is immersed in an oil bath, enters directly into the density determination.

A 125x filar micrometer microscope is used to determine the position of the buoy. A new lens combination, which includes an objective lens (38 mm) with a larger working distance (less power) and a higher-power (14x) eyepiece, gives approximately the same magnification as with the earlier apparatus [1]. The microscope is rigidly mounted on an aluminum support table, adjustable in three dimensions. The entire assembly is secured firmly with bolts to the massive concrete block structure.

### 3.4 Concentric Cylinder Capacitor

The capacitor for dielectric constant measurements was located in the top portion of the sample space, as seen in figure 2. The central support mandrel of the capacitor was connected rigidly to the sample cell lid using a slotted brass tube, crimped at its ends, that clamped tightly over mating surfaces on the mandrel and the lid. The same type of brass tube was used to connect the differential capacitance sensor to a nut at the bottom of the capacitor. The use of the brass tubes for support of the components inside the cell resulted in an extremely rigid assembly that provided means for independent rotational orientation of each component. The coaxial leads to the differential capacitance sensor located below the capacitor passed through the brass tubes and a slot in the central support mandrel of the capacitor.

The concentric cylinder capacitor design used in the present work was based on that developed by Younglove and Straty [23]. Two slightly different capacitors are used with the present apparatus, depending on whether the measurements are for mixtures or for pure fluids. For mixture measurements, slots are cut into the cylinders parallel to the

cylindrical axes, similar to the ring and bar design of Pan et al. [24]. This modification was made to minimize the chances for composition gradients in the cell by allowing free passage of fluid mixtures between the electrodes. The vacuum capacitance of the capacitor with slotted cylinders was approximately 20 pF, while that for the one with solid cylinders was about 33 pF.

The dimensions of the capacitors used here were proportionally the same as those of Younglove and Straty [23]; however, the overall size was significantly smaller. The overall external dimensions of each capacitor were 6.4 cm length  $\times$  1.77 cm diameter. For the capacitor with slots, the widths of the five slots in each cylinder were 0.32 cm, while the slot lengths in the outer cylinder were 4.1 cm and those in the inner cylinder were 1.9 cm. The outside diameter of the inner cylinder was 1.06 cm. The outer cylinder had a thickness of 0.32 cm, while that of the inner cylinder was 0.24 cm. There was a separation distance of 0.38 mm between the cylindrical electrodes. Small pieces of Kapton<sup>2</sup> film (0.05 mm thickness) were used to insulate the electrodes from the support assembly. Both of the capacitors were fabricated from copper. A thin protective coating of gold was flashed over the surfaces.

## 4. Measurements

### 4.1 Temperature and Pressure

The primary temperature sensor, calibrated on the IPTS-68, is a platinum resistance thermometer, which had been used with the previous densimeter [1]. The uncertainty of the calibration is approximately 0.002 K. The potentiometric system for temperature measurements gives uncertainties that range from approximately 0.010 K at 100 K to 0.030 K at 300 K. The temperature of the sample space is regulated within a few mK, approximately the same as the reproducibility of the temperature measurements. A current of 1 mA for the thermometer, supplied by an electronic constant current source, is determined to an uncertainty of approximately 0.002%. The total uncertainty in the measured temperatures is estimated to be less than 0.03 K.

---

<sup>2</sup>In order to describe materials and experimental procedures adequately, it is occasionally necessary to identify commercial products by manufacturers' or trade names. In no instance does such identification imply endorsement by the National Bureau of Standards, nor does it imply that the particular product is necessarily the best available for that purpose.

Vapor pressure measurements on liquid nitrogen, methane, ethane, and propane at temperatures from 100–290 K have been used to check the calibration of the thermometer. Temperatures from vapor pressure measurements, using selected data from the literature, generally agreed with measured temperatures (platinum resistance thermometer) to better than 0.02 K. Further details on temperature measurements are presented in reference [1].

Temperature differences between the ends of the cell are monitored with vapor pressure bulbs located at the ends of the cell. The bulbs have been filled with the fluids mentioned above, the selected fluid depending on the temperature range needed. With the reflux tube evacuated, overall temperature differences were typically less than 0.01 K, or within the precision of the vapor pressure measurements. Thus, a differential thermocouple, with junctions placed near the vapor pressure bulbs, was not needed as part of a control loop to regulate the temperature distribution along the length of the cell.

A third vapor pressure bulb was soldered in close thermal contact with the guard ring. This vapor pressure bulb was used to check a differential thermocouple between the guard ring and the cell. This thermocouple was part of a control circuit to maintain the temperature of the guard ring approximately equal to that of the sample cell. The guard ring was connected to a copper radiation shield that surrounded the cell to provide an approximately isothermal environment for the sample space.

The techniques and instrumentation for control of the temperature of the cell are standard. Four independent heaters along the length of the cell are available, if needed, to minimize temperature gradients. Only the middle two heaters have been used in the control circuit. It should also be noted that temperature gradients along the length of the cell can be monitored by observing the vapor pressure of the liquid inside the cell as a function of the liquid level.

Pressures of the fluid under test are usually measured with a dual-range, precision oil dead-weight gauge. Its sensitivity ranges from  $2 \times 10^{-4}$  MPa at 3 MPa to  $2 \times 10^{-3}$  MPa at 35 MPa. The overall uncertainty in pressure is approximately 0.01%, increasing somewhat at lower pressure. With the high range piston, this gauge cannot be used for pressures less than 0.2 MPa; with the low range piston, the lowest pressure is approximately 0.04 MPa.

A spiral quartz Bourdon-tube gauge with a range of 0–1.38 MPa is normally used for vapor pressure measurements. It has been calibrated against an air dead-weight gauge; maximum uncertainty in the

calibration was 70 Pa. The resolution of this gauge is better than 20 Pa.

Both pressure gauges are characterized by relatively small free volumes, approximately 0.5 cm<sup>3</sup> for each. This is an important consideration when performing mixture (phase equilibria) measurements with this apparatus, e.g., to minimize vapor space corrections.

## 4.2 Density

The accuracy and precision of density measurements with the magnetic suspension technique used here depend on a knowledge of the mass and volume of the buoy, along with the capability to determine the position of the buoy with high resolution independent of the medium in which the buoy is suspended. The same barium ferrite buoy as used with the previous densimeter was employed here; its properties have been well characterized and are discussed elsewhere [1]. The mass of the buoy is 0.73706 g and its volume at 300 K is 0.13485 cm<sup>3</sup>. Thermal expansion data [25] for barium ferrite were previously obtained to calculate the volume of the buoy at low temperatures. The change in the volume of the buoy for a temperature change from 100–300 K is approximately 0.4%.

The earlier densimeter was used at relatively low pressures compared to those used now. Based on the properties of similar materials, it was estimated that the effect of pressure on the volume of the barium ferrite buoy was negligible (<0.001%) for the highest pressures (2.5 MPa) encountered with the previous densimeter. Since the new apparatus is used at pressures up to 35 MPa, bulk modulus measurements [26] have been carried out on a sample of barium ferrite, the buoy material. Bulk modulus ( $B_T$ ) data (in units of MPa) from 75–295 K are represented as a function of temperature ( $T$  in units of K) by the expression,

$$B_T = B_{295} \left( 1.01629 - \frac{0.0206014}{e^{\frac{175.15}{T-75}} - 1} \right), \quad (3)$$

where  $B_{295} = 1.3030 \times 10^5$  MPa, the bulk modulus at 295 K. Coefficients were determined from nonlinear least squares. The correction to the volume of the buoy at room temperature for a pressure of 35 MPa amounts to 0.027%.

For density measurements, it is necessary to suspend the buoy at the same position relative to the support

coil in vacuum and in the test fluid at the same temperature. Although the microscope lens combination (sec. 3.3) used here is different from that of the previous densimeter, the present arrangement results in position measurements of the same quality. The maximum error in the position determination is  $2 \times 10^{-3}$  mm, which corresponds to an error in density of less than 0.03% for a density of  $5 \times 10^2$  kg/m<sup>3</sup>, or larger.

The position of the buoy is observed through a 0.63 cm thick sapphire window in the cell. It has been observed that the apparent position of the buoy changes slowly with the pressure inside the cell; as the cell volume expands, the angle of the sapphire window changes. The magnitude of this effect has been determined as follows. First, the microscope is adjusted so that the position of the buoy is independent of the index of refraction of the fluid inside the cell. This procedure is accomplished by observing the buoy resting at a stationary position on the capacitance sensor assembly as the cell is alternately filled with gas and liquid at a pressure slightly greater than 0.1 MPa; e.g., methane at 120 K. The temperature of the cell is maintained during these tests. Then, the cell is filled with liquid at a pressure less than 0.1 MPa; either propane, isobutane, or normal butane have proved ideal for these tests at temperatures between 100 and 300 K. Then, the pressure inside the cell is increased to greater than 35 MPa while observing the buoy at rest on the sensor assembly. The change in the index of refraction for a 35-MPa change in pressure along an isotherm for liquid propane, isobutane, or normal butane is negligible compared to the change in refractive index in going from vapor-to-liquid for methane at 120 K. The change in position with pressure corresponds to a change in density with pressure of less than  $5 \times 10^{-2}$  kg/(m<sup>3</sup>·MPa) for liquid methane at 120 K.

The currents in the support coil needed to suspend the buoy in vacuum and in the fluid of interest (see eq (1)) are determined by measuring the voltage drops across a 0.5- $\Omega$  standard resistor in series with the support coil. The voltages were routinely measured to  $5 \times 10^{-6}$  V with a high resolution differential-type voltmeter, which corresponds to a change in density of less than 0.01% for a density of  $5 \times 10^2$  kg/m<sup>3</sup>.

## 4.3 Dielectric Constant

The dielectric constant is determined from a measurement of the ratio of the capacitance of the concentric cylinder capacitor with fluid between the electrodes to the capacitance under vacuum. The capacitances are measured with a three-terminal ac

bridge operated at an oscillator frequency of 5 kHz. Measurements to a resolution of  $10^{-6}$  can be obtained with little difficulty with this bridge.

Both capacitors used in this work yielded equal results within the precision of the measurements in tests on liquid methane. Measurements on mixtures are inherently more difficult and are generally characterized by greater scatter because of the difficulties associated with obtaining homogeneous liquid mixtures in the sample space. Examples of dielectric constant measurements on pure fluids and mixtures with the apparatus described here are given in references [7,19–22,27].

Measurements of the vacuum capacitance are normally obtained just before or just after fluid measurements are performed. Since vacuum measurements are required for each run in the density measuring technique used here, there was no reason vacuum capacitances should not be recorded at the same time. Thus, there was no reason to acquire a calibration curve representing the vacuum capacitance as a function of temperature. Vacuum measurements can be made to a precision of  $10^{-4}$  pF and are usually stable within 0.0002 pF when the sample cell is cycled between low temperature and room temperature. (Vacuum capacitances have been observed to be stable to better than  $10^{-3}$  pF for more than 20 temperature cycles over a period of several months.) The total change in the vacuum capacitance from 300–100 K is approximately 0.3%. Based on tests by Younglove and Straty [23] on a similar cylindrical capacitor, the effect of pressure on the capacitor was sufficiently small to neglect. It is estimated that, based on the resolution of the capacitance measurements and the stability of the capacitor design, the total uncertainty in the dielectric constant measurements is approximately 0.01%.

## 5. Performance of Apparatus

### 5.1 Results and Discussion

Before completing measurements for the LNG density project, it was necessary to ensure that the new densimeter yielded results consistent with those from the previous densimeter. First, density data were obtained for several components of LNG (e.g., methane, ethane, etc.); the data obtained with the new apparatus agreed to better than 0.02% with the results [1,3,4] determined at the onset of the LNG density project with the earlier version [1] of the magnetic suspension densimeter. As mentioned earlier, measurements on saturated liquid methane were used as a check on the measurement process during the entirety of the LNG density project. Dielectric

constant data for liquid methane exhibited differences of <0.01% when compared with the data of Straty and Goodwin [28].

Next, data were obtained for a binary mixture of methane and ethane, a system that had been extensively investigated with the earlier densimeter. The data for three mixtures of methane and ethane had been used to optimize several mathematical models [15–18] developed for prediction of LNG densities. The most accurate and versatile of these models was the extended corresponding states method [15–17]. The new data for a methane+ethane mixture would be compared with predictions from this model. The mixture, for which data are reported here, had also been used to cross-check results from this laboratory obtained with the magnetic suspension densimeter with those from another laboratory that employed an entirely different technique for determining density [29]. The experimental density of Miller and Hiza [29] for this methane+ethane mixture at 110.08 K differed by 0.01% from that calculated from the extended corresponding states model [16].

The experimental orthobaric liquid densities, vapor pressures, and dielectric constants of a 0.85147 CH<sub>4</sub>+0.14853 C<sub>2</sub>H<sub>6</sub> mixture are presented as a function of temperature in table 1. Excess volumes and values for the Clausius-Mossotti (CM) function, as well as values for the excess function, are also given in table 1. The excess volume ( $V^E$ ) is defined by the relation,

$$V^E = V - \sum_i x_i V_i [1 + \beta_i (p_i - p)], \quad (4)$$

where  $V$  is the molar volume of the mixture at a given temperature at saturation pressure  $p$ ,  $V_i$  is the molar volume of component  $i$  at the same temperature at saturation pressure  $p_i$ ,  $x_i$  is the mole fraction of component  $i$ , and  $\beta_i$  is the isothermal compressibility of component  $i$ . The CM function is defined by the expression,

$$CM = \frac{1}{\rho} \left( \frac{\epsilon - 1}{\epsilon + 2} \right), \quad (5)$$

where  $\rho$  is the density and  $\epsilon$  is the dielectric constant. Then the excess Clausius-Mossotti function ( $CM^E$ ) for a liquid mixture is defined, analogous to  $V^E$ , by the relation,

$$CM^E = CM - \sum_i x_i CM_i, \quad (6)$$

**Table 1.** Orthobaric liquid densities ( $\rho$ ) and dielectric constants ( $\epsilon$ ) of 0.85147 CH<sub>4</sub>+0.14853 C<sub>2</sub>H<sub>6</sub> mixture (molecular weight=18.1265 g·mol<sup>-1</sup>) as a function of temperature ( $T$ ) and pressure ( $P$ ).  $\rho_{\text{CSM}}$ , density calculated from extended corresponding states model;  $V^{\text{E}}$ , excess volume; CM, Clausius-Mossotti function;  $\text{CM}^{\text{E}}$ , excess Clausius-Mossotti function.

$T$ K	$P$ MPa	$\rho$ mol·dm <sup>-3</sup>	$\frac{10^3(\rho_{\text{expt}}-\rho_{\text{CSM}})}{\rho_{\text{CSM}}}$	$\frac{V^{\text{E}}}{\text{cm}^3\cdot\text{mol}^{-1}}$	$\epsilon$	$\frac{\text{CM}}{\text{cm}^3\cdot\text{mol}^{-1}}$	$\frac{\text{CM}^{\text{E}}}{\text{cm}^3\cdot\text{mol}^{-1}}$
115.00	0.116	25.3618	-0.059	-0.410	1.67297	7.2243	0.005
120.00	0.166	24.9911	-0.013	-0.493	1.66070	7.2220	0.000
125.00	0.232	24.5983	-0.045	-0.567	1.64828	7.2239	-0.001
130.00	0.316	24.1950	-0.036	-0.655	1.63561	7.2258	-0.003

where CM refers to the Clausius-Mossotti function of the mixture at a given temperature at the saturation pressure of the mixture, and CM<sub>*i*</sub> is the Clausius-Mossotti function of pure component *i* at the same temperature and pressure as the mixture. Adjustments of the pure component CM<sub>*i*</sub>'s to the saturation pressure of the mixture are sufficiently small to neglect.

In the calculation of  $V^{\text{E}}$  and CM<sub>*i*</sub>, the pure component molar volumes of methane and ethane were calculated from equations in references [1,3] obtained from fitting experimental orthobaric liquid densities determined with the earlier version of the magnetic suspension densimeter used in the LNG density project. Vapor pressures for methane and ethane were taken from Goodwin [30] and from Goodwin et al. [31], respectively. Isothermal compressibilities for methane were taken from Rowlinson [32]; those for ethane from Miller [33]. The dielectric constants of Straty and Goodwin [28] were used for methane, while those of Weber [34] were used for ethane.

Also presented in table 1 are comparisons between the experimental densities ( $\rho_{\text{expt}}$ ) from this work and densities ( $\rho_{\text{CSM}}$ ) calculated from the extended corresponding states model [15–17]. The average absolute deviation is 0.038%. This result, combined with the pure fluid comparisons, demonstrates that data obtained with the new densimeter are consistent with data taken with the previous instrument. The total uncertainty of a single density measurement for these binary mixture data is estimated to be  $\pm 0.1\%$ . The present results are also consistent within experimental error with the data point of Miller and Hiza [29] for the same mixture.

The calculated excess Clausius-Mossotti values were less than 0.07% of the mixture CM values for the methane+ethane mixture data presented here. This result was expected based on dielectric constant and density measurements on other mixtures containing nonpolar constituents [7,9,24]. It appears that the excess CM values show a slow decrease with

increasing temperature.

After the new apparatus had been thoroughly tested, it was used to complete the measurements for the LNG density project [7,9]. Next, the apparatus was used to obtain data for propane [19–20], isobutane [19,21], and normal butane [19,22] at pressures up to 35 MPa. The performance of the apparatus at high pressures is demonstrated by these pure fluid data.

## 5.2 Error Analysis

Detailed discussions of the systematic and random errors involved in measurements with the magnetic suspension densimeter used in the present work have been presented elsewhere [1,3–9, 19–22]. The uncertainty in the density measurements depends primarily on the uncertainties in the determination of the volume of the buoy, of the relative position of the buoy and the support coil, and of the temperature of the sample fluid. With the new apparatus, designed for higher pressures than the previous one, the effect of pressure on the apparent position of the buoy, resulting from slight movement of the cell window, must now be included. Maximum uncertainty in the density determination resulting from this effect is 0.02%.

The effect of pressure on the volume of the buoy, which is extremely small at maximum design pressure of the cell, must also be considered. As discussed in section 3.3, the reduction in the buoy volume for a pressure of 35 MPa is 0.027%. The uncertainty involved in this adjustment is negligible.

As discussed [1], the total uncertainty of a single density measurement is taken as the square root of the sum of the squares of the systematic errors plus an allowance of three times the standard deviation for random error. The imprecision of measurement (or standard deviation) is typically less than 0.02%. Both the precision and accuracy of density measurements with a magnetic suspension densimeter depend on the difference between the density of the buoy and the

density of the fluid. For the present arrangement, where the density of the buoy is significantly larger (typically an order of magnitude) than the density of the fluids, the precision and total uncertainty change slowly with fluid density. The total systematic error in the measurement process from known sources is approximately 0.05% at low temperatures, decreasing to approximately 0.03% at room temperature. This results in an estimated total uncertainty in the density of approximately 0.1% at low temperatures and 0.06% at room temperature. (Of course, the uncertainty in the density determination also depends on the values of the derivatives,  $(\partial\rho/\partial P)_T$  and  $(\partial\rho/\partial T)_P$ , for the particular region of the PVT surface for the fluid under investigation.)

The uncertainties in the dielectric constant determination have been discussed in detail (sec. 4.3 and refs. [7,9,19-22]). The total uncertainty in the dielectric constant measurement is estimated to be approximately 0.01%.

The estimates of the uncertainties in the density and dielectric constant measurements can be tested to some degree by making comparisons with reliable data from independent sources. Such comparisons have been made for many fluids over wide ranges of experimental parameters (such as temperature, pressure, density, etc.) [7,9,19-22]. In general, these comparisons have confirmed the estimates of the uncertainty levels.

There has been little information presented in this paper concerning the problems associated with mixture measurements compared to pure fluid measurements. The uncertainties involved in the determination of the composition of mixtures have been discussed in detail in previous papers [1,5-9].

The authors are grateful to the following individuals who made significant contributions in the development of this apparatus. W. R. Bjorklund, A. N. DiSalvo, W. G. Layne (deceased), and D. L. Smith assisted in the fabrication of the apparatus. M. J. Hiza participated in many fruitful discussions. H. M. Ledbetter provided prepublished bulk modulus data for barium ferrite.

## 6. References

- [1] Haynes, W. M.; Hiza, M. J.; Frederick, N. V. Magnetic suspension densimeter for measurements on fluids of cryogenic interest. *Rev. Sci. Instrum.* **47**(10): 1237-1250; 1976 October.
- [2] Haynes, W. M. Simplified magnetic suspension densimeter for absolute density measurements. *Rev. Sci. Instrum.* **48**(1): 39-41; 1977 January.
- [3] Haynes, W. M.; Hiza, M. J. Measurements of the orthobaric liquid densities of methane, ethane, propane, isobutane, and normal butane, *J. Chem. Thermodyn.* **9**(2): 179-187; 1977 February.
- [4] Haynes, W. M.; Hiza, M. J. Orthobaric liquid densities of normal butane from 135 to 300 K as determined with a magnetic suspension densimeter. *Advances in Cryogenic Engineering*, Vol. 21. Timmerhaus, K. D.; Weitzel, D. H., ed. New York, NY: Plenum Press; 1976 516-521.
- [5] Hiza, M. J.; Haynes, W. M.; Parrish, W. R. Orthobaric liquid densities and excess volumes for binary mixtures of low molar-mass alkanes and nitrogen between 105 and 140 K. *J. Chem. Thermodyn.* **9**(9): 873-896; 1977 September.
- [6] Hiza, M. J.; Haynes, W. M. Liquid mixture excess volumes and total vapor pressures using a magnetic suspension densimeter with compositions determined by chromatographic analysis: methane plus ethane. *Advances in Cryogenic Engineering*, Vol. 23. Timmerhaus, K. D., ed. New York, NY: Plenum Press; 1976; 594-601.
- [7] Haynes, W. M. Orthobaric liquid densities and dielectric constants of (methane+isobutane) and (methane+normal butane) at low temperatures. *J. Chem. Thermodyn.* to be published.
- [8] Hiza, M. J.; Haynes, W. M. Orthobaric liquid densities and excess volumes for multicomponent mixtures of low molar-mass alkanes and nitrogen between 105 and 125 K. *J. Chem. Thermodyn.* **12**(1): 1-10; 1980 January.
- [9] Haynes, W. M. Measurements of orthobaric-liquid densities of multicomponent mixtures of LNG components ( $N_2$ ,  $CH_4$ ,  $C_2H_6$ ,  $C_3H_8$ ,  $CH_3CH(CH_3)CH_3$ ,  $C_4H_{10}$ ,  $CH_3CH(CH_3)C_2H_5$ , and  $C_5H_{12}$ ) between 110 and 130 K. *J. Chem. Thermodyn.* **14**(7): 603-612; 1982 July.
- [10] Goodwin, R. D. Apparatus for determination of pressure-density-temperature relations and specific heats of hydrogen to 350 atmospheres at temperatures above 14 K. *J. Res. Natl. Bur. Stand. (U.S.)* **65C**(4): 231-243; 1961 October-December.
- [11] Prydz, R.; Straty, G. C. The thermodynamic properties of compressed gaseous and liquid fluorine. *Natl. Bur. Stand. (U.S.) Tech. Note* 392; 1970 October; 182 p.
- [12] Straty, G. C.; Prydz, R. Fluorine compatible apparatus for accurate PVT measurements. *Rev. Sci. Instrum.* **41**(8): 1223-1227; 1970 August.
- [13] Straty, G. C.  $(\rho, V, T)$  of compressed fluid ethene. *J. Chem. Thermodyn.* **12**(8): 709-716; 1980 August.
- [14] Frederick, N. V.; Haynes, W. M. Differential capacitance sensor as position detector for a magnetic suspension densimeter. *Rev. Sci. Instrum.* **50**(9): 1154-1155; 1979 September.
- [15] McCarty, R. D. A comparison of mathematical models for the prediction of LNG densities. *Natl. Bur. Stand. (U.S.) NBSIR* 77-867; 1977 October. 60 p.

- [16] McCarty, R. D. Four mathematical models for the prediction of LNG densities. *Natl. Bur. Stand. (U.S.) Tech. Note* 1030; 1980 December. 76 p.
- [17] McCarty, R. D. Mathematical models for the prediction of liquefied-natural-gas densities. *J. Chem. Thermodyn.* **14**(9): 837-854; 1982 September.
- [18] Hiza, M. J. An empirical excess volume model for estimating liquefied natural gas densities. *Fluid Phase Equilibria* **2**(2): 27-38; 1978 August.
- [19] Haynes, W. M.; Younglove, B. A. Dielectric constants of saturated liquid propane, isobutane, and normal butane. *Advances in Cryogenic Engineering*, Vol. 27. Fast, R. W., ed. New York, NY: Plenum Press; 1982. 883-891.
- [20] Haynes, W. M. Measurements of densities and dielectric constants of liquid propane from 90 to 300 K at pressures to 35 MPa. *J. Chem. Thermodyn.* to be published.
- [21] Haynes, W. M. Measurements of densities and dielectric constants of liquid isobutane from 120 to 300 K at pressures to 35 MPa. *J. Chem. Eng. Data.* to be published.
- [22] Haynes, W. M. Measurements of densities and dielectric constants of liquid normal butane from 140 to 300 K at pressures to 35 MPa. *J. Chem. Thermodyn.* to be published.
- [23] Younglove, B. A.; Straty, G. C. A capacitor for accurate wide range dielectric constant measurements on compressed fluids. *Rev. Sci. Instrum.* **41**(7): 1087-1089; 1970 July.
- [24] Pan, W. P.; Mady, M. H.; Miller, R. C. Dielectric constants and Clausius-Mossotti functions for simple liquid mixtures: systems containing nitrogen, argon and light hydrocarbons. *AIChE J.* **21**(2): 283-289; 1975 March.
- [25] Clark, A. F.; Haynes, W. M.; Deason, V. A.; Trapani, R. J. Low temperature thermal expansion of barium ferrite. *Cryogenics* **16**(3): 267-270; 1976 May.
- [26] Ledbetter, H. M. Fracture and Deformation Division, National Engineering Laboratory, National Bureau of Standards, Boulder, CO 80303. private communication.
- [27] Haynes, W. M.; McCarty, R. D. Prediction of liquefied-natural-gas (LNG) densities from dielectric constant measurements. *Cryogenics.* to be published.
- [28] Straty, G. C.; Goodwin, R. D. Dielectric constant and polarizability of saturated and compressed fluid methane. *Cryogenics* **13**(12): 712-715; 1973 December.
- [29] Miller, R. C.; Hiza, M. J. Experimental molar volumes for some LNG-related saturated liquid mixtures. *Fluid Phase Equilibria* **2**(1): 49-57; 1978 August.
- [30] Goodwin, R. D. The thermophysical properties of methane, from 90 to 500 K at pressures to 700 bar. *Natl. Bur. Stand. (U.S.) Tech. Note* 653; 1974 April; 274 p.
- [31] Goodwin, R. D.; Roder, H. M.; Straty, G. C. Thermophysical properties of ethane, from 90 to 600 K at pressures to 700 bar. *Natl. Bur. Stand. (U.S.) Tech. Note* 684; 1976 August. 319 p.
- [32] Rowlinson, J. S. *Liquid and Liquid Mixtures*. 2nd Ed. London: Butterworths; 1969. 51.
- [33] Miller, R. C. Estimating the densities of natural gas mixtures. *Chem. Eng.* **81**(23): 134-135; 1974 October.
- [34] Weber, L. A. Dielectric constant data and the derived Clausius-Mossotti function for compressed gaseous and liquid ethane. *J. Chem. Phys.* **65**(1): 446-449; 1976 July.

# An Intercomparison of Pressure Standards Between the Istituto di Metrologia "G. Colonnetti" and the National Bureau of Standards

J. C. Houck, G. F. Molinar, and R. Maghenzani  
National Bureau of Standards, Washington, DC 20234

Accepted: April 26, 1983

Intercomparisons were performed between a primary standard gas piston gauge of the Istituto di Metrologia "G. Colonnetti" (IMGC) and two gauges at the National Bureau of Standards. The agreement between the average pressure generated by the IMGC primary standard and the NBS transfer gauge was within 7 ppm (over the range 0.75 to 5.0 MPa) and the agreement between the IMGC primary standard and the NBS primary standard was within 6 ppm (over the range 0.5 to 1.5 MPa). The agreement is well within the estimated uncertainties of the gauges: 24 ppm for the IMGC primary gauge, 30 ppm for the NBS transfer gauge, and 28 ppm for the NBS primary gauge.

Key words: effective area; intercomparison; piston gauge; pressure; primary standard; transfer standard.

Intercomparisons of pressures generated by a primary standard gas piston gauge (IMGC5) of the Istituto di Metrologia "G. Colonnetti" were made with pressures generated by a transfer gas piston gauge (PG23) of NBS and a primary standard gas piston gauge (PG24) of NBS.

A rather comprehensive treatment of piston gauges is given by Heydemann and Welch [1].<sup>1</sup> With the permission of the authors, selected portions of this treatment are modified and presented as background for readers not familiar with piston gauges. Pressure is defined as force per unit area and its value can be determined by a direct force-per-unit area measurement with a piston gauge. A *primary* standard piston gauge is one for which the area is determined by direct di-

dimensional measurements. A *transfer* standard piston gauge is one for which the area is determined by intercomparison with another piston gauge or or monometer.

The pressure is applied to the end face of a piston of known cross sectional area and the resulting force is measured by loading the piston with weights. Figure 1 is a schematic cross section of a piston gauge showing a vertical piston, which in operation is supported by the applied pressure balancing the force due to gravity acting on the piston, the weight carrier, and the weights.

The pressure  $p$  generated by a piston gauge at its reference level is given by eq (1)

$$p = \frac{\sum_{i=1}^n M_i g (1 - \rho_{\text{air}} / \rho_{M_i}) + \gamma C + T_w}{A_0 [1 + (\alpha_c + \alpha_p)(T - T_{\text{ref}})] [1 + bp]} \quad (1)$$

where the symbols have the following meanings:

$M_i, \rho_{M_i}$  mass and density of weight  $i$ ,  
 $\rho_{\text{air}}$  density of air at the temperature, barometric pressure, and humidity prevailing in the laboratory,

**About the Authors:** J. C. Houck is with the Temperature and Pressure Measurements and Standards Division, NBS, and NBS guest workers G. F. Molinar and R. Maghenzani have returned to IMGC, Strada delle Cacce 73, 10135, Torino, Italy.

<sup>1</sup> Figures in brackets indicate the literature references at the end of this paper.

$\gamma$	surface tension of pressure-transmitting fluid,
$C$	circumference of the piston where it emerges from the fluid,
$T_w$	tare weight or error,
$A_0$	effective area of the assembly at zero pressure,
$\alpha_c, \alpha_p$	thermal expansivities of cylinder and piston,
$T$	temperature of the assembly,
$T_{ref}$	temperature to which $A_0$ is referred,
$b$	pressure coefficient of the effective area.

The term  $(1 - \rho_{air}/\rho_M)$  is the air buoyancy correction for weight  $i$ .  $\gamma C$  is the force exerted on the piston by the surface tension of the fluid. The term  $[1 + (\alpha_c + \alpha_p)(T - T_{ref})]$  corrects the area for thermal expansion. The term  $[1 + bp]$  describes the change of the effective area with pressure. This important correction term will be the one discussed in this article. Several effects contribute to the change of effective area with pressure: the distortion of the piston under the combination of the longitudinal stress due to the applied load and the hydrostatic pressure over part of its length; and the distortion of the cylinder due to the internal pressure over part of its length, and external pressure and end-loading where applicable.

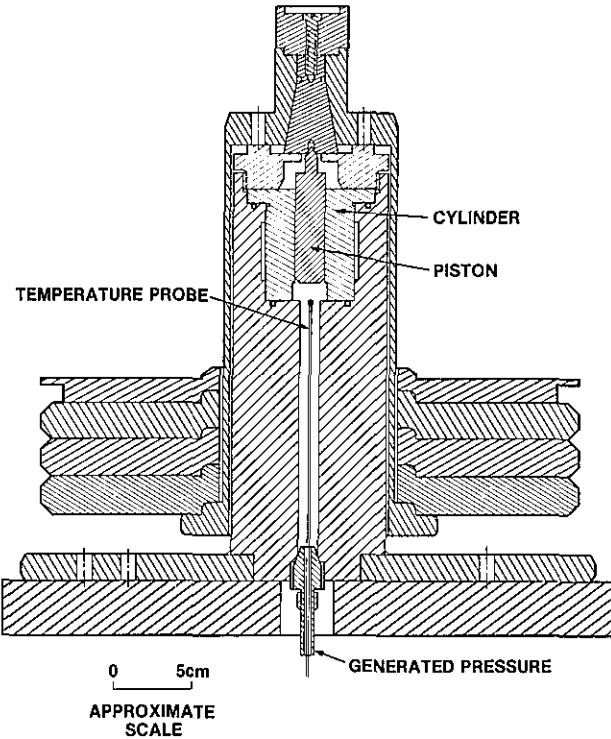


Figure 1-IMGC5 simple piston and cylinder dead weight piston gauge. The temperature probe is a thermocouple referenced to 0 °C. For this figure as well as figures 2 and 3, the piston and cylinder materials are given in table 1; the shadings in the figures do not indicate the materials of the components.

Several authors have made significant contributions to the calculation of these distortions. See reference [1] for more details and additional references. The change in radius  $r_p$  of a solid piston subjected to end pressure  $p$ , surrounded by the pressure  $p_c$  in the clearance is given according to Johnson and Newhall [2] by

$$\frac{r_p(p) - r_p(0)}{r_p(0)} = \frac{\mu p}{E} + \frac{p_c}{E} (\mu - 1) \quad (2)$$

where  $\mu$  is Poisson's ratio and  $E$  is the modulus of elasticity. The change in the radius  $r_c$  of a hollow cylinder of outside radius  $R_c$  is given by

$$\begin{aligned} \frac{r_c(p) - r_c(0)}{r_c(0)} = & \frac{p_c}{E} \left[ \frac{(1 + \mu)R_c^2 + (1 - \mu)r_c^2}{R_c^2 - r_c^2} \right] \\ & - \frac{p_0}{E} \left[ \frac{2R_c^2}{R_c^2 - r_c^2} \right] + \frac{\mu p_c}{E} \quad (3) \end{aligned}$$

where  $p_0$  is the pressure on the outside of the cylinder, and  $p_c$  is the pressure on the end faces.

In eqs (2) and (3),  $p_c$  varies along the piston from a maximum at the lower end to zero at the top of the cylinder, and the exact correction for piston and cylinder distortion depends on the geometry of the clearance. In practice the geometry of the clearance may change with pressure.

The effective area is the arithmetic mean between the areas of the piston and of the cylinder

$$A_{eff} = 1/2(A_p + A_c) \quad (4)$$

Equations (2) and (3) can now be introduced into eq (4), and, assuming for simplicity that  $p_c = 0.5 p$ , we have for the pressure coefficient  $b$  of eq (1)

$$\begin{aligned} b = & -(1 - 3\mu)/2E_p \quad (\text{piston distortion}) \\ & + \{(1 + \mu_c)R_c^2 + (1 - \mu_c)r_c^2\} / \{2E_c(R_c^2 - r_c^2)\} \\ & \quad (\text{cylinder distortion due to internal pressure}) \\ & - (p_0/pE_c)\{2R_c^2/(R_c^2 - r_c^2)\} \\ & \quad (\text{cylinder distortion due to external pressure}) \\ & + (p_c/p)(\mu_c/E_c) \\ & \quad (\text{cylinder distortion due to end loading}) \quad (5) \end{aligned}$$

Let us get an estimate for the size of these corrections to the area. For steel  $E = 2 \times 10^{11}$  N/m<sup>2</sup> and  $\mu = 0.28$ ; further let  $R_c/r_c = 3$  and we have for the pressure coefficient

$$\begin{aligned} b_{steel} = & -4 \times 10^{-13} + 38 \times 10^{-13} - 112 \times 10^{-13} (p_0/p) \\ & + 14 \times 10^{-13} (p_c/p) \quad (6) \end{aligned}$$

**Table 1.** Main characteristics of the three piston gauges used in the intercomparison.

Piston gauge designation	IMGC5	NBS-PG23	NBS-PG24
Piston-cylinder type	Simple	Partially re-entrant	Controlled-clearance
Piston material, cylinder material	Tungsten-carbide, tool steel	Tungsten-carbide, tungsten carbide	Tungsten-carbide, tool steel
Fluid	Dry nitrogen	Dry nitrogen	Dry nitrogen
Range (MPa)	0.5–5.0	0.7–5.0*	0.5–1.5
Reference temperature (°C)	23	23	23
Effective area $A_0$ at atm. pressure and at 23 °C (m <sup>2</sup> )	$2.000662 \times 10^{-4}$	$8.390170 \times 10^{-6}$	$5.067132 \times 10^{-4}$
Pressure coefficient (MPa <sup>-1</sup> )	$1.0 \times 10^{-6}$	0.0*	$-5.1 \times 10^{-7}$
Thermal coefficient of expansion $\alpha_p$ for piston (°C <sup>-1</sup> )	$5.5 \times 10^{-6}$	$4.55 \times 10^{-6}$	$4.9 \times 10^{-6}$
Thermal coefficient of expansion $\alpha_c$ for cylinder (°C <sup>-1</sup> )	$12.0 \times 10^{-6}$	$4.55 \times 10^{-6}$	$12.0 \times 10^{-6}$
Total estimated relative uncertainty of the pressure <sup>†</sup> ( $\Delta p/p$ ) (ppm)	24.0	30.0	28.0

\* NBS-PG23 has a range 0.7 to 17.2 MPa but the zero pressure coefficient is applicable only in the range 0.7 to 5.0 MPa.

† Total estimated uncertainty includes uncertainties of effective area at atm. pressure and 23 °C, pressure coefficient, thermal expansion coefficients of piston and cylinder, gravity, and masses.

all in m<sup>2</sup>/N.

For cemented tungsten carbide with  $E=6 \times 10^{11}$  N/m<sup>2</sup> and  $\mu=0.2$  the pressure coefficient is

$$b_{TC} = -3.4 \times 10^{-13} + 12 \times 10^{-13} - 38 \times 10^{-13} (p_0/p) + 3 \times 10^{-13} (p_c/p) \quad (7)$$

all in m<sup>2</sup>/N. It is immediately obvious that, depending on the design of the gauge, the pressure coefficient can be positive, negative, or even zero. Different ways of dealing with the pressure coefficient  $b$  have led to the design of various types of piston gauges—three different ones were used in this intercomparison. Table 1 gives the relevant characteristics of each of the gauges.

Figure 1 is a schematic cross section of IMGC5, a simple piston and cylinder in which the effective area at atmospheric pressure (determined from the average of the areas of the piston and of the cylinder) was obtained from direct dimensional measurements of the

diameters. The pressure coefficient of the effective area ( $b=1.0 \times 10^{-6}$  MPa<sup>-1</sup>) used in these intercomparisons was determined by IMGC by comparison with another IMGC simple piston and cylinder gas piston gauge of 2 MPa range whose pressure coefficient had been calculated theoretically.

Figure 2 is a schematic cross section of NBS-PG23 which has a partially re-entrant piston and cylinder with the effective area at atmospheric pressure and the pressure coefficient determined by comparison with a primary standard. PG23 has a pressure range of 0.7 to 17.2 MPa and was calibrated against the primary standard PG24, but only over the range of 0.7 to 1.9 MPa. From this calibration we obtained a value for  $A_0$  and concluded that  $b \approx 0.0$ . On a theoretical basis the pressure coefficient would be expected to be between  $-2.4 \times 10^{-6}$  MPa<sup>-1</sup> (the calculated value for the lower re-entrant half of the piston and cylinder) and  $+0.7 \times 10^{-6}$  MPa<sup>-1</sup> (calculated for the upper half of the piston and cylinder which behaves like a simple piston and cylinder). Future comparisons with NBS gauges

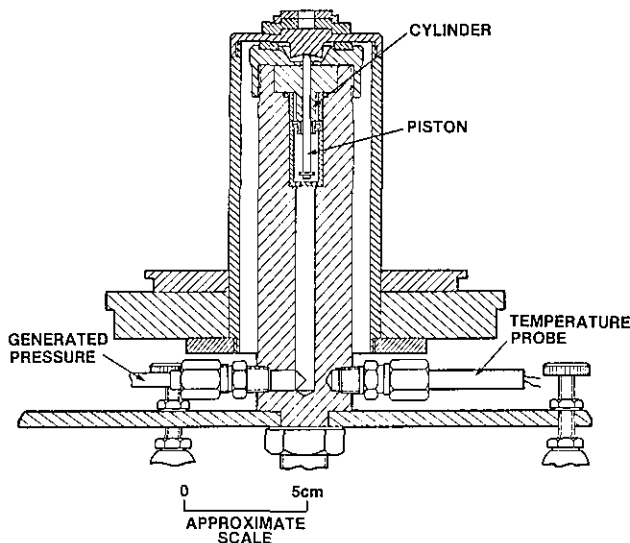


Figure 2—NBS-PG23 partially re-entrant piston and cylinder dead weight piston gauge. The temperature probe is a 100-ohm Platinum Resistance Thermometer (PRT).

operating at higher pressures will give a value of the pressure coefficient for PG23 to use over a greater range than was used for this intercomparison.

Figure 3 is a schematic cross section of NBS-PG24 which is a primary standard controlled-clearance piston gauge with the effective area derived from di-

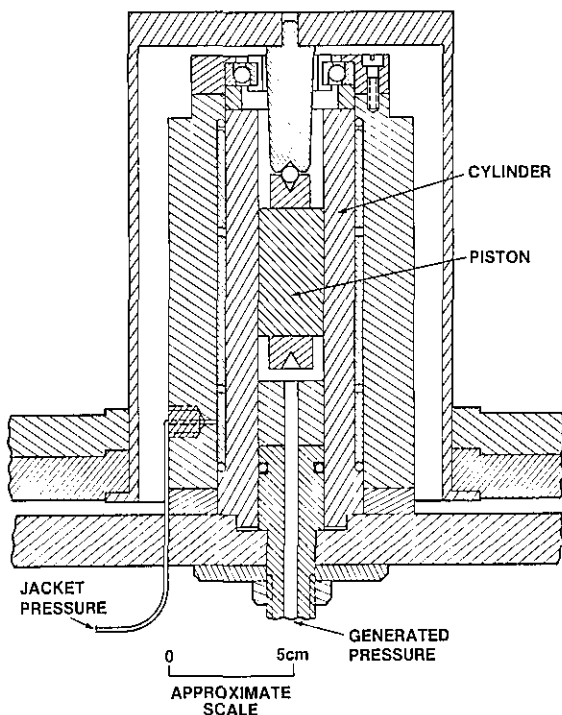


Figure 3—NBS-PG24 controlled-clearance dead weight piston gauge. A 100-ohm platinum resistance thermometer for temperature measurement was mounted on the base plate at a position not shown in the figure.

dimensional measurements of the piston only, with an empirically determined correction based on extrapolation of jacket pressure required to close the cylinder on the piston, and a theoretical pressure coefficient ( $-5.1 \times 10^{-7} \text{ MPa}^{-1}$ ) applied to the deformation of the piston only.

The calculations for pressure measurements by controlled-clearance piston gauges, and by other types of piston gauges, as well as considerations of direct comparison, are also given by Heydemann and Welch [1]. Dry nitrogen was used as the pressure fluid. A pressure head correction for nitrogen was applied for the difference in level between the bottom of pistons of the gauges at their operating levels. The gauges were operated at temperatures near  $23^\circ\text{C}$ . Using the thermal expansion coefficients given in table 1, the effective areas were corrected for the operating temperature. The pistons were manually rotated in the CW direction at a frequency between 0.5 to 2.0 Hz.

Electronic position indicators were used to monitor the vertical position of each gauge while determining the pressure balance to ensure that each gauge was used at its correct operating height. The rate of change of position was used to determine that the rate of fall was appropriate for indicating that the pressures were balanced during the intercomparison.

A total of 21 comparisons at 10 different pressures was made between IMGC5 and NBS-PG23. One method of evaluating the data was to regard PG23 as the standard and IMGC5 as a test gauge to be calibrated using the NBS computer program for calibrating test gauges. This program determines the effective area and the pressure coefficient of the test gauge in terms of those of the standard.

In eq (8),  $p$  is the pressure generated at the reference level of the test instrument by the standard gauge.

$$p = \frac{F^T}{A_0^T(1 + b_1^T p + b_2^T p^2)} \quad (8)$$

where

$$F^T = \frac{Mg[1 - (\rho_{\text{air}}/\rho M)] + \gamma C + T^T}{1 + (\alpha_p + \alpha_c)(T - T_r)} \quad (9)$$

is the force exerted on the test gauge piston,  $A_0^T$  is the effective area of the test gauge,  $b_1^T$  is the fractional change of effective area with pressure of the test gauge, and  $b_2^T$  is the fractional change of effective area of the test gauge with the square of the pressure.

Note that for simplicity the temperature correction of the area has been lumped with the force,  $F^T$ .

The RHS of eq (8) represents the pressure generated

by the test gauge at its reference level. By adjusting  $F^T$  this pressure is made equal to  $p$ . The effective area  $A_0^T$  and the coefficients  $b_1^T$  and  $b_2^T$  can then be obtained by fitting

$$F^T = A_0^T p (1 + b_1^T p + b_2^T p^2) - T^T \quad (10)$$

to the  $(F^T, p)$  data obtained from the comparisons.

If eqs (11-18) are fitted to the data at very low pressures, the terms involving the pressure coefficients  $b_1$  and  $b_2$  are usually insignificant and either eq (11) or (12) is used to characterize the gauge. Note that  $T$  may be either a tare error or a coefficient necessary to characterize the behavior of the gauge properly. At higher pressures the coefficient  $b_1$  and occasionally also  $b_2$  become significant and must be included in the function fitted to the data.

$$F^T = p A_0^T \quad (11)$$

$$F^T = p A_0^T - T \quad (12)$$

$$F^T = p A_0^T (1 + b_1^T p) \quad (13)$$

$$F^T = p A_0^T (1 + b_1^T p) - T \quad (14)$$

$$F^T = p A_0^T (1 + b_1^T p + b_2^T p^2) \quad (15)$$

$$F^T = p A_0^T (1 + b_1^T p + b_2^T p^2) - T \quad (16)$$

$$F^T = p A_0^T (1 + b_2^T p^2) \quad (17)$$

$$F^T = p A_0^T (1 + b_2^T p^2) - T \quad (18)$$

A high-speed digital computer will perform these computations in a few seconds and, apart from the coefficients, will determine the standard deviations of the coefficients, the residual standard deviations, and the residuals. A plot of the residuals as functions of pressure will show at a glance whether any gross errors have been made in recording and entering the data.

The proper fit is finally selected by comparing the residual standard deviations of the various fits and the standard deviations of the coefficients. The standard deviation of the residuals is reduced as more coefficients are used to characterize the gauge. However, since the number of degrees of freedom is reduced simultaneously, the uncertainty of the coefficients increases. Selected, therefore, is the fit with the least

number of coefficients, which gives low residual standard deviation and for which each coefficient is greater than three times the standard deviation of the coefficient. The lowest order eq (11) ( $F = pA$ ) was selected and gives an effective area of the IMGC gauge of  $2.000661 \times 10^{-4} \text{ m}^2$  at  $23^\circ \text{C}$  with a standard deviation of the area of 0.6 ppm. The area of the IMGC gauge given by IMGC is  $2.000662 \times 10^{-4} \text{ m}^2$  at  $23^\circ \text{C}$ . The areas are seen to differ by 0.5 ppm which is less than one standard deviation.

Another method of evaluating the intercomparison was to calculate the pressure generated by each piston gauge according to the method used by the respective laboratories. The results of the 21 direct comparisons (the same points used in the first method) are shown in table 2. The pressures were referenced to the base of the IMGC piston to account for head corrections. The average of the pressures calculated by IMGC minus the pressures calculated by NBS is  $-12.7 \text{ Pa}$  with a standard deviation of the mean of  $2.0 \text{ Pa}$ . The average of the pressures calculated by IMGC minus the pressures calculated by NBS divided by the NBS

Table 2. Comparison of pressures measured by IMGC5 and by NBS-PG23 piston gauges in chronological order.

Pressure defined by		Pressure difference	Pressure difference
IMGC5 (MPa)	NBS-PG23 (MPa)	IMGC5 - NBS-PG23 (Pa)	Pressure difference Pressure IMGC5-NBS-PG23 NBS PG23 (ppm)
.750184	.750193	- 9	-12.0
2.998337	2.998362	-25	- 8.3
4.996813	4.996836	-23	- 4.6
4.996824	4.996845	-21	- 4.2
3.997585	3.997591	- 6	- 1.5
2.998342	2.998356	-14	- 4.7
1.999101	1.999100	1	.5
.999861	.999865	- 4	- 4.0
.750184	.750200	-16	-21.3
1.499478	1.499485	- 7	- 4.7
2.498710	2.498724	-14	- 5.6
3.497947	3.497975	-28	- 8.0
4.497188	4.497202	-14	- 3.1
4.497188	4.497217	-29	- 6.5
3.997576	3.997591	-15	- 3.7
3.497947	3.497969	-22	- 6.3
2.498711	2.498713	- 2	- .8
1.999101	1.999111	-10	- 5.0
1.499478	1.499483	- 5	- 3.3
.999862	.999861	1	1.0
.750183	.750188	- 5	- 6.7
Mean value		-12.7	- 5.4
Standard deviation of the mean		2.0	1.0

pressure is -5.4 ppm with a standard deviation of the mean of 1.0 ppm.

Sixteen comparisons were made between IMGC5 and NBS-PG24 at five different pressures. The same lowest order eq (11) ( $F=pA$ ) was selected for this pair of gauges. It gives an effective area of the IMGC gauge of  $2.000649 \times 10^{-4} \text{ m}^2$  at 23 °C with a standard deviation of the area of 0.6 ppm. The difference in area of the IMGC gauge determined by this NBS standard (NBS-PG24) in this comparison with that given by IMGC is -6.5 ppm. The second method of evaluating the intercomparisons was also applied to this pair of gauges. The results of the 16 direct comparisons are shown in table 3. The average of the pressures calculated by IMGC minus the pressures calculated by NBS is -6.8 Pa with a standard deviation of the mean of 1.1 Pa. The average of the pressures calculated by IMGC minus the pressures calculated by NBS divided by the NBS pressures is -6.5 ppm with a standard deviation of the mean of 0.6 ppm.

Figure 4 is a plot of the differences in pressure calculated from the characteristics of the gauges versus pressure, and figure 5 is a plot of the *relative* difference in pressure calculated from the characteristics of the gauges versus pressure. While a systematic difference

**Table 3.** Comparison of pressures measured by IMGC5 and by NBS-PG24 piston gauges in chronological order.

Pressure measured by		Pressure difference	<u>Pressure difference</u>
IMGC5	NBS-PG24	IMGC5 NBS-PG24	<u>Pressure</u>
(MPa)	(MPa)	(Pa)	<u>IMGC5-NBS-PG24</u>
			<u>NBS PG24</u>
			(ppm)
.750240	.750244	- 4	- 5.3
.999918	.999927	- 9	- 9.0
1.249856	1.249868	-12	- 9.6
1.499533	1.499539	- 6	- 4.0
1.499534	1.499547	-13	- 8.7
1.249855	1.249861	- 6	- 4.8
.999917	.999925	- 8	- 8.0
.750238	.750242	- 4	- 5.3
.750238	.750242	- 4	- 5.3
.999917	.999924	- 7	- 7.0
1.249854	1.249866	-12	- 9.6
1.499532	1.499547	-15	-10.0
.500319	.500321	- 2	- 4.0
.500319	.500322	- 3	- 6.0
.500319	.500321	- 2	- 4.0
.500318	.500320	- 2	- 4.0
Mean value		- 6.8	- 6.5
Standard deviation of the mean		1.1	0.6

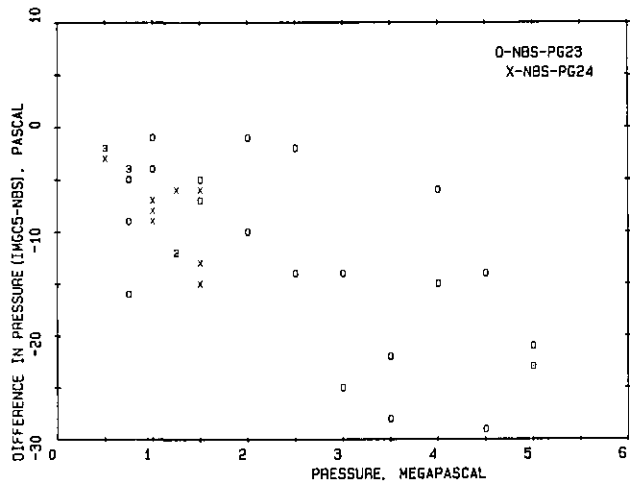


**Figure 4**—Difference in pressure (Pa) versus pressure (MPa) for IMGC5 against NBS-PG23 and IMGC5 against NBS-PG24. The numbers “2” and “3” represent the number of replicate data for IMGC5 against NBS-PG24 plotted at the same point.

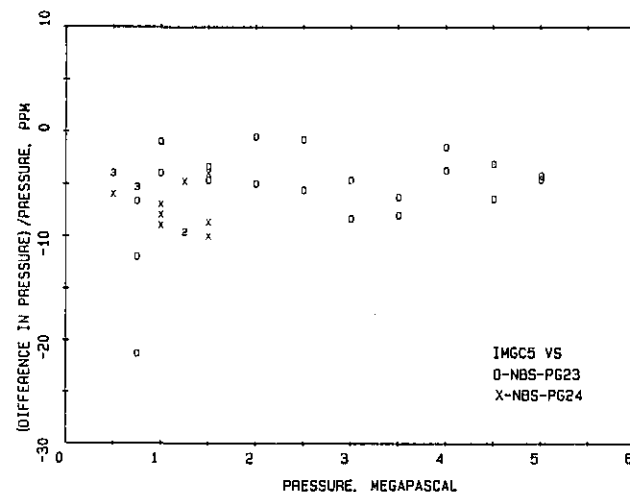


**Figure 5**—Difference in pressure divided by pressure (ppm) versus pressure (MPa) for IMGC5 against NBS-PG23 and IMGC5 against NBS-PG24. The numbers “2” and “3” represent the number of replicate data for IMGC5 against NBS-PG24 plotted at the same point.

in pressure is evident in the data, it is small compared to the estimated systematic uncertainties.

Both methods of expressing the results of the intercomparisons show significantly better agreement between the gauges (1 to 7 ppm) than the estimated systematic uncertainty of each of the gauges (IMGC5, 24 ppm; NBS-PG23, 30 ppm; and NBS-PG24, 28 ppm).

The differences observed between IMGC5 and NBS-PG24 (the primary standard), 6.8 ppm by area comparison and 6.5 ppm by pressure comparison, indicate that the two different methods of calculating

effective areas are well verified at this pressure range. The differences observed, between IMGC5 and NBS-PG23, the transfer standard, 0.5 ppm by area comparison and 5.4 ppm by pressure comparison, indicate that the latter gauge serves very well as a transfer standard in the given pressure range.

## References

- [1] Heydemann, P. L. M.; Welch, B. E. Experimental thermodynamics of non-reacting fluids. Vol. II, Chapter 4, Part 3. *Piston Gages*, Editors: LeNeindre and Vodar, Butterworths; 1975.
- [2] Johnson, D. P.; Newhall, D. H. *Trans. Amer. Soc. Mech. Engrs.* 75, 301 (1953).

# Analysis of Liquid Flow-Induced Motion of a Discrete Solid in a Partially Filled Pipe

Bal M. Mahajan

National Bureau of Standards, Washington, DC 20234

Accepted: April 20, 1983

An analysis is presented for the liquid flow-induced motion of a solid in partially filled pipes. A general equation of the flow-induced motion of a solid is developed. Two alternate force models, one ( $F_v$ ) based on free stream velocity and another ( $F_m$ ) based on free stream momentum flux, are formulated to simplify the general equation.

The equation of motion is solved for the motion of a cylindrical solid with steady-uniform liquid flows and the effects of relevant variables on the motion of a solid are predicted. The variables considered include: volume rate of liquid flow,  $Q$ ; pipe diameter,  $D$ ; Manning coefficient,  $n$ ; and slope,  $S$ ; solid diameter,  $d$ ; length,  $L$ ; specific gravity,  $\sigma$ ; coefficient of friction between a solid and the pipe wall,  $\eta$ ; and the two force functions,  $F_v$  and  $F_m$ .

The flow rate,  $Q$ , required to initiate the motion of a solid increases with an increase in  $D$ ,  $n$ ,  $d$ ,  $L$ ,  $\sigma$ , and  $\eta$ , and decreases with an increase in  $S$ . The force function  $F_m$  predicts a lower value of  $Q$  than does the force function  $F_v$ .

The velocities of a solid increase with an increase in  $Q$  and  $S$  and decrease with an increase in  $D$ ,  $n$ ,  $d$ ,  $L$ ,  $\sigma$ , and  $\eta$ . The force function  $F_m$  predicts higher values of the velocity of a solid than does the force function  $F_v$ .

The effects of the variables  $Q$ ,  $D$ ,  $S$ ,  $d$ ,  $L$ , and  $\eta$  on the velocities of a solid are qualitatively consistent with the available experimental data. The qualitative agreement between the predicted results and experimental data demonstrate the validity of the analysis presented.

Key words: analysis; flow; force; liquid; model; momentum; partially-filled; pipe; solid; solid-liquid channel flow; steady; uniform; velocity.

## 1. Introduction

The transport of solids by flowing liquids falls into three different categories: (1) the sediment transport in rivers and canals—the sediment particles usually move on the river bed and do not block the passage of the flow or alter the cross-sectional area of the flow; (2) the pipeline transport of finite solids and particle suspensions by full-bore liquid flows—the flow parameters (velocity, volume flow rate, and pressure) of the carrier liquid are relatively easy to obtain since the pipe is completely filled with the liquid; (3) the pipeline transport of solids by flowing liquids only partially filling the pipe (open channel flows)—the flow parameters (velocity, volume rate of flow, and flow depth) of carrier liquid are relatively difficult to obtain. (The difficulty is encountered even for a constant volume flow rate because the flow velocity and depth may vary along the length of the pipe; furthermore, the transported solid may substantially alter the flow area and the solid may or may not be fully submerged.)

**About the Author:** Bal M. Mahajan is a mechanical engineer in the NBS Center for Building Technology.

## Nomenclature

<p><math>A</math> = flow cross-sectional area</p> <p><math>A_s</math> = cross-sectional area of solid</p> <p><math>A_{sw}</math> = wetted portion of the cross-sectional area of the solid</p> <p><math>A_w</math> = portion of the pipe's cross-sectional area occupied by the water, or the flow cross-sectional area</p> <p><math>C_l</math> = lift coefficient</p> <p><math>C_r</math> = coefficient of flow-induced force</p> <p><math>d</math> = diameter of the solid</p> <p><math>D</math> = diameter of the pipe</p> <p><math>E</math> = flow specific energy</p> <p><math>F_b</math> = buoyant force</p> <p><math>F_f</math> = friction force</p> <p><math>F_l</math> = lift force</p> <p><math>F_m</math> = force function based on free stream momentum flux</p> <p><math>F_p</math> = pressure force</p> <p><math>Fr</math> = Froude number</p> <p><math>F_s</math> = shear force</p> <p><math>F_v</math> = force function based on free stream velocity</p> <p><math>F_{ws}</math> = flow-induced thrust force acting on the solid</p> <p><math>g</math> = acceleration due to gravity</p> <p><math>h</math> = depth of water stream</p> <p><math>L</math> = length of the solid</p> <p><math>m</math> = mass of the solid</p> <p><math>n</math> = the Manning coefficient</p> <p><math>P_w</math> = wetted perimeter</p> <p><math>P_{sw}</math> = wetted perimeter of the solid</p> <p><math>p</math> = pressure</p> <p><math>Q</math> = volume flow rate</p> <p><math>R</math> = <math>A/P_w</math> = hydraulic radius</p> <p><math>R_n</math> = normal reaction, force due to pipe wall acting on the solid in a direction perpendicular to the pipe axis</p> <p><math>S</math> = pipe slope = <math>\sin\theta</math></p> <p><math>S_f</math> = energy gradient or slope of the energy line</p> <p><math>T</math> = time</p> <p><math>U</math> = solid velocity</p>	<p><math>V</math> = water velocity</p> <p><math>V_{wd}</math> = volume of water displaced by the solid</p> <p><math>W_b</math> = buoyed weight of the solid</p> <p><math>W_s</math> = weight of the solid</p> <p><math>X_s</math> = axial distance traversed by a solid</p> <p><math>x</math> = x-axis or the axial distance along the length of the pipe</p> <p><math>y</math> = y-axis or the distance perpendicular to the pipe axis</p> <p style="text-align: center;"><i>Greek Symbols</i></p> <p><math>\alpha</math> = acceleration</p> <p><math>\gamma</math> = specific weight</p> <p><math>\eta</math> = friction coefficient</p> <p><math>\epsilon</math> = <math>y/d</math> and/or <math>h/d</math></p> <p><math>\theta</math> = pipe slope angle</p> <p><math>\lambda</math> = <math>y/D</math> and/or <math>h/D</math></p> <p><math>\nu</math> = <math>V_o - U_m</math></p> <p><math>\rho</math> = density</p> <p><math>\sigma</math> = specific gravity</p> <p><math>\tau_{sw}</math> = average value of shear stress due to water flow on the solid</p> <p style="text-align: center;"><i>Subscripts</i></p> <p>m refers to maximum value</p> <p>o refers to free stream condition</p> <p>p, <math>p</math> refers to pipe or pressure</p> <p>s refers to solid</p> <p>t refers to instantaneous values</p> <p>v refers to free stream quantity</p> <p>1 refers to nose or upstream end of the solid</p> <p>2 refers to tail or downstream end of the solid</p>
---	--

The first two categories of solid transport by flowing liquids have been investigated extensively [1,2]<sup>1</sup>, while the third category has received relatively little attention. Situations involving the transport of solids with partially filled pipe flows are common occurrences in gravity drainage systems and in some aspects of the chemical industry.

Recently, transport of discrete solids in partially filled pipes was experimentally investigated at the National Bureau of Standards (NBS) [3,4]. In these experiments, single cylindrical solids were transported by unsteady (surge type) water flows in slightly pitched horizontal pipes and the effects of selected variables on the velocity ( $U_s$ ) of the solid were examined. The variables considered in the experiments were: the volume of water ( $V_w$ ) used in an experiment, diameter ( $D$ ) and slope ( $S$ ) of the pipe, diameter ( $d$ ) and length ( $L$ ) of the solid, and the coefficient of static friction ( $\eta_s$ ) between the solid and the pipe wall. The data of these experiments indicated that: (1) at any given cross-section of the pipe,  $U_s$  increases with an increase in  $V_w$  and  $S$ , and a decrease in  $D$ ,  $d$ ,  $L$ ,  $\eta_s$ ; (2)  $U_s$  first increases, apparently reaches a maximum value, and then starts to decrease as the solid travels downstream; and (3) the difference between the local maximum velocity ( $V_m$ ) of water and the  $U_s$  appears to be a function of the axial distance from the solid's starting location and all of the selected variables.

Recent experimental studies at NBS and in several foreign countries [3-8] have enhanced the understanding of the water flow-induced motion of discrete solids in partially filled pipes. These studies have also revealed the complexities of the mechanism of momentum exchange between the liquid and solid and the dissipation of flow energy. Formulation and selection of rational momentum exchange or force models are essential steps for developing techniques for predicting the motion or transport of discrete solids in partially filled pipes under all flow conditions.

This paper presents an analysis of the liquid flow-induced motion of a discrete solid in a partially filled pipe. Various forces acting on the solid are discussed and a general equation for the axial motion of the solid is developed.

This general equation is also shown to be applicable to the liquid flow-induced motion of a discrete solid in a pipe flowing full. Two simplified force models are formulated. The simplified equation is used to study the motion of a finite cylindrical solid for steady-uniform flows. The effects of utilizing different force models and of relevant variables on the various states of the motion of the solid are examined. The variables considered for this parametric study include the following: volume rate of steady uniform flow; coefficient of friction between the solid and the pipe wall; variables of the pipe (i.e., pipe diameter, slope, and the Manning coefficient); and the variables of the solid (i.e., diameter, length, and specific gravity).

The three states of the motion of the solid investigated are: (1) the threshold conditions, i.e., the effects of the variables on the threshold flow rate or the minimum value of flow rate required to initiate the motion of a solid are examined; (2) the acceleration of a solid from rest to the equilibrium velocity, i.e., the effects of the variables on the velocity of a solid along the length of the pipe are examined; and (3) the equilibrium conditions, i.e., the effect of the variables on the equilibrium velocity of the solid are examined.

## 2. Analysis

### 2.1 Types of Partially Filled Pipe Flows

Before considering the transport of a solid by liquid in partially filled pipes (or open channel flows in pipes), it is instructive to briefly describe the types of open channel flows that may occur in nominally horizontal or slightly pitched horizontal pipes. Partially filled pipe flows are classified as: steady or unsteady according to the changes in flow parameters with respect to time,  $T$ , and uniform or varied according to the changes in flow parameters with respect to distance,  $x$ , along the length of the pipe [9,10]. In general, there are three basic types of partially filled pipe flows: (1) steady-uniform flows; (2) steady-varied flows; and (3) unsteady or unsteady-varied flows.

<sup>1</sup> Figures in brackets indicate literature references at the end of this paper.

Establishment of unsteady-uniform flows is practically impossible [9,10]. Also, considering the effects of gravity the state of a partially filled pipe flow may be subcritical (Froude number,  $Fr$ , less than unity), critical ( $Fr$  equal to unity), or supercritical ( $Fr$  greater than unity). These three basic types of flow can be further described as follows:

*Steady-uniform flows.* The flow parameters, that is volume flow rate or discharge  $Q$ , depth  $h$ , and velocity  $V$ , do not vary with respect to both  $T$  and  $x$ . Also, the energy line, water surface, and pipe axis are parallel. Any one of the flow parameters ( $Q$ ,  $h$ , or  $V$ ) completely define the flow conditions for a given pipe, i.e., if  $Q$  is given,  $h$  and  $V$  can be easily determined by the use of the Chezy or Manning formula [9,10].

*Steady-varied flows.* The flow may be either gradually or rapidly varied. For steady varied flows,  $Q$  is constant with respect to both  $T$  and  $x$ , but  $h$  and  $V$  are constant only with respect to  $T$  and vary with  $X$ . The energy line, water surface, and pipe axis are not parallel. There are several (about 12 for gradually varied flows) possible water surface profiles or flow profiles for steady varied flows. For given value of  $Q$  through a pipe, values of  $h$  and  $V$  at any section of the pipe may be determined by numerical integration of the steady-varied flow equations.

*Unsteady flows.* Unsteady flows may be either gradually varied unsteady flows or rapidly varied unsteady flows. Short duration unsteady flows through slightly-pitched-pipes, as in horizontal branches of gravity drainage systems when a plumbing fixture is discharged into the drains serving the fixture, are often called surge flows. For surge flows, the volume flow rate of the liquid entering the pipe rises rapidly from zero to a peak value, and then gradually falls off to zero. A surge flow attenuates as it moves downstream, i.e., the peak values of the flow parameters decrease with an increase in axial distance from the pipe inlet.

For unsteady flow, the flow parameters vary with both  $T$  and  $x$ . Also, the energy line, water surface, and pipe axis are not parallel. Owing to their complexity, the exact solutions of the unsteady flow equations are not possible. However, various finite difference schemes have been developed to obtain approximate solutions of the unsteady flow equations. Numerical integration techniques applying the method of characteristics may be used to estimate the attenuation of a surge flow along the length of the pipe and to obtain approximate values of the flow parameters [5,9–13].

The application of such finite difference techniques has been the subject of a parallel study at NBS to investigate the motion of solids in partially filled pipes [8]. In this approach, motion of the solid is predicted by an empirical equation linking the disturbed flow depth across the solid to its velocity and other flow parameters. The flow-induced motion of a solid predicted by this technique is qualitatively consistent with the observed data.

## 2.2 Description of Liquid-Solid Interaction and the Motion of a Solid

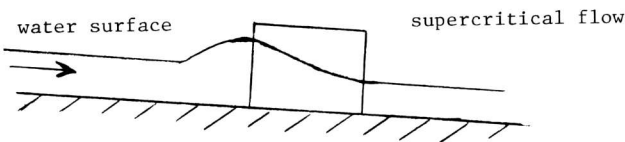
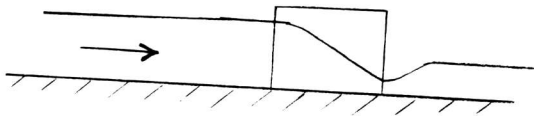
Let us visualize what happens in the case of a single cylindrical solid, initially at rest in a slightly pitched horizontal pipe, as a partially filled pipe flow approaches the solid. The stationary solid partially blocks the flow and the liquid rushes through the crescent shaped space between the solid and the pipe wall. In addition, when an open channel flow is obstructed by the presence of an obstacle (such as a bridge pier, dam, sluice gate, or a weir), the depth of the liquid surface upstream of the obstacle becomes greater than it would have been for unobstructed flow. This phenomenon is called the “backwater” effect of the obstruction on the flow and has been studied by many researchers, see, for example, references [9] and [10].

The extent of this effect is greatly dependent upon the size of the obstruction and the state of the flow. Flow at the obstruction is either subcritical or supercritical [9,10]. For example, if the obstructed flow is subcritical, the backwater will extend a long distance upstream relative to the dimensions of the obstruction (fig. 1). If the flow is supercritical and the obstruction is relatively small, the water surface adjacent to the upstream end of the obstruction is disturbed and the disturbance does not extend further upstream. However, a relatively large obstruction may cause the upstream water level to rise above the critical depth and cause the backwater effect to extend

a short distance upstream (fig. 1); this backwater profile may be terminated by a hydraulic jump. The backwater effect of solids on the flow was observed during the recent experimental study by the author [3,4]; this effect is shown in figure 2.

As a result of the backwater effect, there is a buildup of some water upstream of the solid causing a hydrostatic head difference along the solid. Also, curvature of the stream lines around the upstream end (or the nose) of the solid may increase the flow velocity at that point. Eddies may be formed along the sides and in front (downstream) of the solid as indicated in figure 3.

The stationary solid, in addition to its weight, is also subjected to the following water flow-induced forces in the downstream direction: (1) a pressure force due to the unequal water depth and unequal velocity along the opposite ends of the solid; and (2) a shear force due to the streaming of water past the solid. The solid is also subjected to similar forces due to the induced air flow in the pipe; the effect of air flow related forces, however, is negligibly small. In addition, the solid is also subjected to a buoyancy force, a reaction force at the solid-pipe contact surface, and a force due to the friction between the solid and the pipe wall.

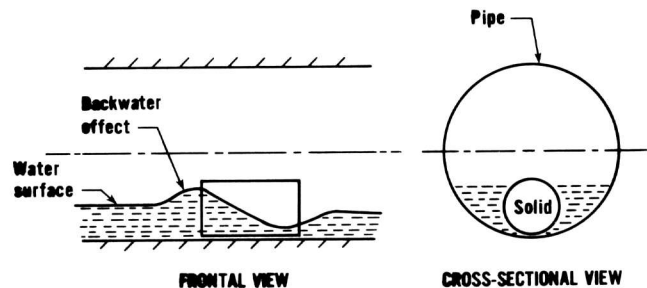
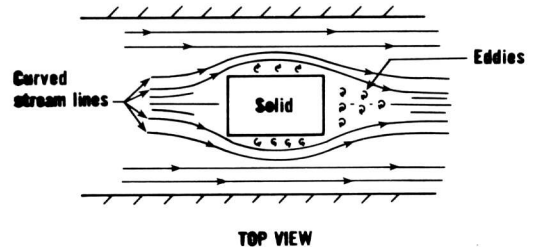
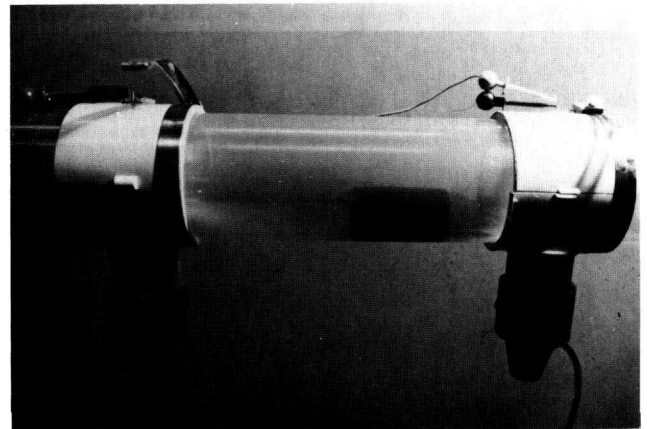


(Clockwise from above)

**Figure 1**—Schematic of the backwater effect of an obstruction on an open channel flow.

**Figure 2**—Photograph showing the “backwater effects” of a solid on the partially-filled pipe flow.

**Figure 3**—Schematic of a cylindrical solid in a partially-filled pipe flow showing eddies and backwater effects.



The result of these forces may not act at the solid's center of gravity, thus producing a net moment which may cause a slight upward tilt of the nose of the solid, a slight lateral displacement of the solid, or both. Any shift in the position of the solid would cause changes in the magnitude and in the line of action of the forces acting on the solid. As a result, the solid may oscillate with respect to its original position for a while or it may take up a new position so that the net moment is zero. However, for the force analysis of the flow-induced motion of the solid it will be assumed that the axis of the solid remains parallel to the pipe axis.

The magnitude of the liquid flow-induced forces acting on the solid increases with an increase in the liquid flow rate through the pipe. The solid remains stationary until the sum of forces acting in the downstream direction exceeds the force due to static friction between the solid and the pipe wall. Once this friction force is exceeded, the solid starts to move. The instantaneous water flow rate, which is just sufficient to start the motion of the solid, is called the "threshold flow rate," and corresponding flow parameters are called "threshold flow parameters."

When the solid is in motion, the friction force is reduced because the coefficient of sliding friction is less than that of static friction. The pressure and shear forces acting on the solid in the downstream direction are also reduced because of a decrease in relative velocity between the water and the solid. The shear force over some parts of the solid surface may even reverse in direction if the solid velocity is higher than the local liquid velocity. This situation is likely to occur near the interface between the bottom of the pipe and the solid. The eddies along the side of the solid and the flow in the thin water layer between the solid and pipe invert may also give rise to a lift force, causing a further reduction in the friction force. As a consequence, the solid accelerates and/or decelerates until it attains an "equilibrium velocity" and a balance of forces develops. The "equilibrium velocity" of the solid (except for steady-uniform liquid flows), does not have a constant value because the velocity of the carrier fluid for steady-varied and surge flows is not constant along the length of the pipe. During the motion of the solid, if the solid velocity is not equal to the local liquid velocity, the liquid continues to flow past the solid.

The solid will continue to move with the equilibrium velocity as long as there is sufficient liquid influx to balance the forces acting on the solid. However, if the flow of carrier fluid through the pipe is of steady-varied or surge flow type, then the liquid flow-induced forces acting on the solid may decrease as the solid moves downstream due to a decrease in the liquid velocity, liquid depth, or both. As a consequence of the decrease in the forces, the solid decelerates, from equilibrium velocity and may come to rest.

In general, there are three different phases of liquid flow-induced motion of a solid in partially filled pipes: (1) the solid accelerates from rest to equilibrium velocity; (2) the solid continues to move at the equilibrium velocity; and (3) the solid decelerates from the equilibrium velocity, particularly if the carrier fluid flow is of steady-varied or surge flow type.

### 2.3 Force Balance and Equations of Motion

The analysis presented below is one-dimensional and deals with the water flow-induced motion of the solid in the downstream direction. Also, it is assumed that the axis of the solid remains parallel to the pipe axis, i.e., any shift of the position of the solid with respect to the pipe axis is neglected.

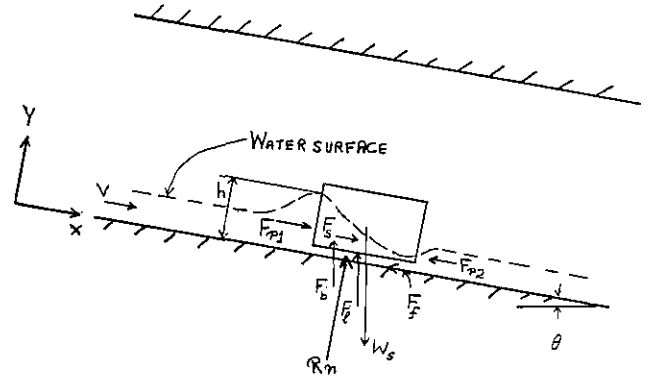
Various forces acting on a cylindrical solid due to water flow in a partially filled pipe were described in the previous subsection. These forces and the coordinate axes are shown in figure 4. Summation of  $x$ - and  $y$ -component of forces yield the following:

$$\Sigma F_x = F_{p1} - F_{p2} + F_s + W_s \sin\theta - F_f - F_b \sin\theta - F_l \sin\theta = ma \quad (1)$$

$$\Sigma F_y = R_n - W_s \cos\theta + F_b \cos\theta + F_l \cos\theta = 0 \quad (2)$$

where the symbols are defined in the nomenclature. The brief descriptions and mathematical formulations of the force terms are given below.

Figure 4—Forces acting on a solid in a pipe flowing only partially full.



The buoyant force,  $F_b$ , is taken equal in magnitude to the weight of water displaced by the solid. (Due to local flow acceleration,  $F_b$  may actually be somewhat less than the weight of the displaced liquid.) It acts in a vertical direction and its line of action passes through the centroid of the volume of water,  $V_{wd}$ , displaced by the solid. Both the magnitude of  $F_b$  and the location of its line of action will vary with the variations in the magnitude and shape of  $V_{wd}$ . Since the stream depth varies along the length of the solid, the magnitude of  $F_b$  may be expressed as:

$$F_b = \rho g \int_{x_1}^{x_2} A_{sw} dx = \rho g V_{wd} = \rho g L \bar{A}_{sw} \quad (3)$$

where  $\bar{A}_{sw}$  = the value of the wetted cross-sectional area of the solid averaged over  $L$  (the length of the solid).

The friction force,  $F_f$ , is due to the friction between the solid and the pipe wall in the presence of water. The value of  $F_f$  is at maximum when the motion of the solid is impending. The magnitude of  $F_f$  decreases when the solid starts to move because the coefficient of dynamic friction is less than that of static friction. The magnitude of  $F_f$  will decrease further if a lift force is generated and it will be equal to zero when  $R_n$  is zero. The value of  $F_f$  may be found as:

$$F_f = \eta R_n, \text{ or substituting } R_n \text{ from eq (2)}$$

$$F_f = \eta \{ (W_s - F_b) - F_\ell \} \cos \theta = \eta (W_b - F_\ell) \cos \theta \quad (4)$$

where

$$W_b = (W_s - F_b) = \rho g L [\sigma A_s - \bar{A}_{sw}] \quad (5)$$

The lift force,  $F_\ell$ , depends on the water solid interaction. It is due to the flow-produced forces on the solid in a direction upward from the pipe wall. Its magnitude and center of action will depend upon the density and size of the solid, the size of the pipe, and the local characteristics of the flow. Force  $F_\ell$  may be assumed to act in a direction parallel to  $F_b$  and it further reduces the magnitude of  $W_b$ . The magnitude of  $F_\ell$  may be assumed to vary between zero to a maximum value of  $W_b$ . The force  $F_\ell$  may be written as:

$$F_\ell = C_\ell W_b \quad (6)$$

where  $C_\ell$  is a lift coefficient which is a function of the flow velocity relative to the solid. The value of  $C_\ell$  varies between zero and one; however at the present state of knowledge,  $C_\ell$  cannot be predicted from theory alone.

The pressure forces  $F_{p1}$  and  $F_{p2}$ , respectively, act on the nose (upstream end) and tail (downstream end) of the solid. The magnitude of pressure forces is dependent on the water depth which is dependent upon the size of the pipe, depth of the flow stream, and the relative velocity between the solid and water. The pressure forces  $F_{p1}$  and  $F_{p2}$  may be written as follows:

$$F_{p1} = \rho g [\bar{y} + U_r^2/2g]_1 A_{sw1} \quad (7)$$

$$F_{p2} = \rho g [\bar{y} + U_r^2/2g]_2 A_{sw2} \quad (8)$$

where subscripts 1 and 2, respectively, refer to the nose and tail of the solid.

$U_r = V - U =$  relative velocity between the solid and the water

$\bar{y}$  = the distance from the water surface to the centroid of the wetted cross-sectional area of the solid,  $A_{sw}$ .

For a right circular cylindrical solid situated with its axis parallel to the axis of the pipe as shown in figure 3,  $\bar{y}$  may be expressed as:

$$\bar{y} = \left( \int_0^h y dA_{sw} \right) / A_{sw} = d \{ [2d^2(\epsilon - \epsilon^2)^{3/2} / 3A_{sw}] - (1 - 2\epsilon) / 2 \} \quad (9)$$

where

$$A_{sw} = \int_0^h dA_{sw} = [\cos^{-1}(1 - 2\epsilon) - 2(1 - 2\epsilon)\sqrt{\epsilon - \epsilon^2}] d^2 / 4 \quad (10)$$

$\epsilon = y/d$ , and  $y$  equal to the distance of the water surface from the bottom of the solid. If the solid is in contact with the pipe, then  $\bar{y}$  may also be expressed as:

$$\bar{y} = \left[ \int_0^h y dA_w \right] / A_w = D \{ [2D^2(\lambda - \lambda^2)^{3/2} / 3A_w] - (1 - 2\lambda) / 2 \} \quad (11)$$

and

$$A_w = \int_0^h dA_w = [\cos^{-1}(1 - 2\lambda) - 2(1 - 2\lambda)\sqrt{1 - \lambda^2}] D^2 / 4 \quad (12)$$

where  $\lambda = h/D$ , and  $h$  is the distance of the water surface from the bottom of the pipe.

The net pressure force,  $F_p$ , acting on the solid in the downstream direction (or  $x$ -direction) may be obtained as:

$$F_p = F_{p1} - F_{p2} = \rho g \{ [\bar{y} + U_r^2/2g]_1 A_{sw1} - [\bar{y} + U_r^2/2g]_2 A_{sw2} \} \quad (13)$$

The shear force  $F_s$  acts over the entire wetted surface of the solid in a direction parallel to the direction of flow. The shear force is dependent upon the size of the solid, the surface roughness of the solid, the depth of flow stream, relative velocity between the solid and the water, and water viscosity. The shear force  $F_s$  may be expressed in a formulation similar to the formulation of the shear force acting on the flow due to pipe friction (or boundary layer shear). The velocity and depth of flow varies along the length of the solid, and  $F_s$  may be formulated in terms of the average values of the variables averaged over the length of the solid as:

$$F_s = \tau_{sw} L \bar{P}_{sw} \quad (14)$$

where

$$\bar{P}_{sw} = \frac{1}{L} \int_{x_1}^{x_2} P_{sw} dx = \cos^{-1}(1 - 2\epsilon) d = \text{average value of wetted perimeter of the solid, averaged over}$$

$L$ , and

$\tau_{sw}$  = average value of shear stress due to water flow on the solid.

The relationship of the shear stress,  $\tau_{sw}$ , to the local flow parameters is not known and needs development.

Substituting the expressions for various force terms from eqs (3), (4), (5), (13), and (14), the equations of motion for the solid may be rewritten as:

$$\rho\{[g\bar{y} + U_r^2/2]_1 A_{sw1} - [g\bar{y} + U_r^2/2]_2 A_{sw2}\} + \tau_{sw} L \bar{P}_{sw} + W_b \sin\theta(1-C_r) - \eta W_b \cos\theta(1-C_r) = m\alpha \quad (15)$$

Equation (15) is free from any assumption regarding the shape or size of the solid or the type of liquid flow in the pipe. Various terms have been formulated for a right circular cylindrical solid in motion or at rest in a pipe partially filled with flowing water; however, eq (15) gives the force balance on a discrete solid of any shape or size moving or at rest in a pipe totally filled or partially filled with flowing liquid.

For example let us examine the case of a right circular cylinder at rest in a pipe filled with flowing liquid; for this case.

$$\alpha = 0, C_r = 0,$$

$$A_{sw1} = A_{sw2} = \pi d^2/4,$$

$$\bar{y}_1 = \bar{y}_2 = d/2,$$

$$\bar{P}_{sw} = \pi d,$$

$$U_{r1} = V_1, U_{r2} = V_2 \text{ and}$$

$$(V_1^2 - V_2^2)/2 = \Delta P \text{ across the solid.}$$

Now substituting these values in eq (15) we get

$$\rho \Delta P A_s = \tau_{sw} L P + W_b \sin\theta - \eta W_b \cos\theta \quad (16)$$

Equation (16), when adjusted for proper direction of various forces, is identical to eq (12-54) of reference [2]. For a cylindrical solid moving with a steady speed in a pipe filled with flowing liquid, eq (15) becomes identical to eq (12-71) of reference [2], after proper directions of the forces are taken into consideration.

#### 2.4 Force Models to Simplify the Equation of Motion

Equation (15) may be further simplified by combining the flow-induced pressure and shear forces to obtain a longitudinal flow-induced thrust force acting on the solid as:

$$F_{ws} - W_b(1-C_r)[\eta \cos\theta - \sin\theta] = m\alpha \quad (17)$$

where,

$$F_{ws} = F_p + F_s = \rho C_f [U_{r1}^2] A_{sw1} / 2 \quad (18)$$

and where  $C_f$  is a coefficient of the flow-induced force acting on the solid and is expressed by the following:

$$C_f = (2/U_{r1}^2 A_{sw1}) [g\bar{y} + U_r^2/2]_1 A_{sw1} - (g\bar{y} + U_r^2/2)_2 A_{sw2} + \tau_{sw} L \bar{P}_{sw} \quad (19)$$

To further simplify eq (19), the force  $F_{ws}$  and the buoyed weight,  $W_b$ , of the solid may be expressed:

$$F_{ws} = \rho C_f [U_{ro}^2/2] A_{swo} \quad (20)$$

$$W_b = \rho g L [\sigma A_s - A_{swo}] \quad (21)$$

where

$$U_{ro} = V_o - U$$

$A_{swo}$  = area of the nose of the solid wetted by the free stream depth,  $h_o$  defined as the stream depth corresponding to the free stream velocity  $V_o$ .

The quantity  $V_o$  is the "free stream velocity," that is, the average velocity of water in the absence of a solid. For a steady uniform flow,  $V_o$  is the free stream velocity of flow in the pipe; for a steady (constant flow rate) gradually varied flow,  $V_o$  is the free stream velocity at location  $x_1$ ; i.e., the axial distance corresponding to the position of the nose of the solid in the pipe; and for an unsteady, or surge flow,  $V_o$  is the free stream velocity at location  $x_1$  and at time  $T_1$ , i.e., the time at which the nose of the solid is at location  $x_1$ .

The quantity  $C_f$  is a coefficient of thrust based on the "free stream velocity." The coefficient  $C_f$  is similar to a well known quantity  $C_d$ , "the coefficient of drag," for submerged bodies in infinite flow streams; here the subscript  $r$  is used to emphasize the thrust force exerted by the flowing liquid on the solid and the finite size of the flow field. Also, the effects of a solid on an infinite flow field are negligible and the drag coefficient,  $C_d$ , is taken as independent of the quantity  $A_{swo}/A_{wo}$  (i.e., the ratio of the wetted cross-section area of the solid and the free stream flow area). Depending on the cross-section areas, the effect of a solid on a partially filled pipe flow may be substantial and should be taken into consideration. Hence, the thrust force coefficient  $C_f$  is considered to be dependent upon the quantity  $A_{swo}/A_{wo}$ .

The exact relationship between  $C_f$  and  $A_{swo}/A_{wo}$  is complex even for a steady uniform flow condition. The approximate value of  $F_{ws}$  may be obtained by assuming that the coefficient  $C_f$  can be expressed as:

$$C_f = 1 + A_{swo}/A_{wo} \quad (22)$$

Substituting  $C_f$  from eq (22) into eq (20),  $F_{ws}$  or  $F_v$  may be expressed as:

$$F_{ws} = F_v = \rho [1 + A_{swo}/A_{wo}] [U_{ro}^2/2] A_{swo} \quad (23)$$

where  $F_v$  is the flow-induced force acting on the solid, the subscript  $v$  is used to indicate that the force is based upon free stream velocity.

The validity of the assumed expression for  $C_d$  may be examined by considering the following two limiting conditions: (a) the solid in an infinite flow field; and (b) the solid completely blocking the flow.

For the first case, when  $A_{w0} \rightarrow \infty$ ; then  $A_{swo}/A_{w0} \rightarrow 0$ . In this case,

$$F_v \rightarrow \rho[U_{ro}^2/2] A_{swo} \quad (24)$$

Equation (24) represents the approximate value of the drag force acting on the cylinder in an infinite flow field with its axis parallel to the free stream velocity, since  $C_d$  for such a cylinder is nearly equal to unity [13].

For the second case, when  $A_{swo} \rightarrow A_{w0}$ ; then  $A_{swo}/A_{w0} \rightarrow 1$ . In this case,

$$F_v = \rho[U_{ro}^2] A_{swo} \quad (25)$$

Equation (25) represents the case of a jet impinging on a flat plate, where the force acting on the solid (i.e., the flat plate) is equal to the total flow momentum relative to the solid [14,15].

Substituting for  $W_b$  and  $F_v$  from eqs (21) and (23), respectively, the equation of motion for the solid, i.e., eq (17) may be rewritten as:

$$\rho(1 + A_{swo}/A_{w0})(U_{ro}^2/2) A_{swo} - \rho g L (\sigma A_s - A_{swo}) [\eta \cos \theta - \sin \theta] (1 - C_d) = m a \quad (26)$$

An alternate expression for the longitudinal flow-induced force,  $F_{ws}$ , acting on the solid may be obtained by considering the "momentum flux" or "specific force,"  $M$ , of the free stream impinging on the solid as discussed below.<sup>2</sup> The momentum flux,  $M$ , of an open channel flow is defined as:

$$M = [\int y dA + QV/g] = (\bar{v} + V^2/g) A_w \quad (27)$$

Force  $F_{ws}$  may be expressed as

$$F_{ws} = F_m = \rho g (\bar{v} + U_{ro}^2/g) A_{swo} - F_2 \quad (28)$$

where  $F_m$  is the flow-induced force acting on the solid, the subscript  $m$  is used to indicate that the force function is based upon the free stream momentum flux, and  $F_2$  represents the force acting on the downstream end of the solid.

When  $U_s = 0$ ,  $U_{co} = V$  and

$$F_{ws} = F_m = \rho g (\bar{v} + V^2/g) A_{swo} - F_2 \quad (29)$$

The first term on the right-hand side of eq (29) represents the force of an open channel flow on an obstruction, such as a sluice gate or a bridge pier, if the force  $F_2$  is negligible. Such a situation is likely to occur only initially when the flowing liquid first contacts the solid. However, as soon as some liquid flowing through the crescent shaped space between the solid and the pipe wall reaches the downstream end of the solid, the liquid fills the portion of the pipe cross-section adjacent to the bottom of the pipe to form a region of eddies as shown in figure 3. The velocity

<sup>2</sup> The quantity  $M$  has been variously called the "momentum flux," the "specific force," the "momentum function," the "total force," the "force plus momentum," or briefly the "force" of a stream [9,10].

relative to the solid of the liquid adjacent to the downstream end of the solid is zero; the depth of this liquid is smaller than the free stream depth except when the buoyed weight of the solid is zero. When the buoyed weight of the solid is equal to zero then the depth of liquid adjacent to the downstream end of the solid is equal to the free stream depth. Hence, it may be assumed that the force  $F_2$  is a hydrostatic force having a value equal to a fraction of the free stream hydrostatic force as:

$$F_2 = \rho g \left( \frac{A_{swo}}{\sigma A_s} \right) \bar{y} A_{swo}. \quad (30)$$

Substituting  $F_2$  from eq.(30) into eq (28), eq (28) may be rewritten as:

$$F_m = F_{ws} = \rho g \left( 1 - \frac{A_{swo}}{\sigma A_s} \right) \bar{y}_o A_{swo} + \rho U_{ro}^2 A_{swo}. \quad (31)$$

The first term on the right-hand side of eq (31) is equal to the net hydrostatic force acting on the solid and is equal to zero when  $W_b$  is equal to zero.

Substituting for  $W_b$  and  $F_{ws}$ , respectively, from eqs (21) and (31), eq (17) may be rewritten as:

$$\rho g \left( 1 - \frac{A_{swo}}{\sigma A_s} \right) A_{swo} + \rho U_{ro}^2 A_{swo} - \rho g L (\sigma A_s - A_{swo}) [\eta \cos \theta - \sin \theta] (1 - C_r) = m \alpha. \quad (32)$$

A comparison of eqs (23) and (31) indicates that at identical flow conditions, the magnitude of force  $F_m$  is larger than that of force  $F_v$ .

Considering the force and mass balance for the water over the length of the pipe,  $L$ , containing the solid, the continuity and momentum equations for water may be expressed as follows:

$$\text{continuity, } Q_1 - Q_2 = \partial / \partial T \int_{x_1}^{x_2} A dx = (\partial A / \partial T) L; \quad (33)$$

$$\text{momentum, } \rho g (M_1 - M_2) + \rho g \bar{A}_w \sin \theta L - \rho g \bar{A}_w L S_f - F_{sw} = -\rho \frac{\partial}{\partial T} (A_w V) L \quad (34)$$

where

$$M = (\bar{y} + V^2/g) A_w,$$

$$S_f = \tau_{pw} / \gamma R = V^2 / C^2 R = n^2 V^2 / R^{4/3},$$

$$\rho g A L \sin \theta = W_w \sin \theta$$

$\tau_{pw}$  = average shear stress due to pipe on the water flow,

and

$F_{sw} = -F_{ws}$  = the flow resistive force exerted by the solid, and  $F_{ws}$  has already been defined in eqs (18), (23), or (31).

Now, if the solid is of infinitesimal length, then eqs (33) and (34) take up the more familiar forms, i.e., the equation for unsteady flow in open channels, e.g.,

when,

$L = \Delta x \rightarrow dx$ , then

$$\partial Q / \partial x + \partial A / \partial T = 0 \quad (35)$$

or

$$\rho \partial M / \partial x + \rho g \bar{A}_w (S_o - S_f) - \partial (F_{sw}) / \partial x = -\rho \partial Q / \partial T. \quad (36)$$

Also, the resistance due to the solid may be expressed in a manner similar to the flow resistance due to the pipe wall as:

$$\partial (F_{sw}) / \partial x = \rho g A_w S_{fs}$$

and eq (23) may be rewritten as:

$$\rho \partial M / \partial x - \rho g \bar{A}_w (S_o - S_f - S_{fs}) = -\rho \partial Q / \partial T \quad (37)$$

where  $S_{fs}$  may be expressed in a manner similar to  $S_f$ , as

$$S_{fs} \approx \bar{U}_r^2 / C_s^2 R \approx n_s^2 U_r^2 / R^{4/3},$$

however, in this case coefficients  $C_s$  and  $n_s$  are not constant and are not known. In the absence of a solid, eq (37) becomes

$$\rho g \partial M / \partial x + \rho \partial Q / \partial T = \rho g A_w (S - S_f) \quad (38)$$

For steady uniform partially filled pipe flows, parameters,  $Q$ ,  $V$ , and  $h$ , are constant throughout the pipe; and for a given value of  $Q$ , the values of  $u$  and  $h$  can be determined using the Manning equation [9,10]. Also, for given values of  $Q$ , pipe variables ( $D, n, S$ ), and solid variables ( $d, L, \sigma$ ), the force  $F_{ws}$  varies only with the solid velocity and eqs (26) and (32) can be integrated in closed form.

For steady-varied and unsteady flows, eqs (35) and (38) may be solved numerically to yield the free stream flow depth and velocity along the length of the pipe. From this solution local values of  $F_{ws}$  and  $W_b$  can be obtained and substituted in eqs (26) and (32). Equations (26) and (32) can also be solved numerically. The numerical solutions of these equations are beyond the scope of this study. However, the effects of relevant variables on various states of the solid motion may be examined, without loss of generality, for steady-uniform partially filled pipe flows. The solutions of eqs (26) and (32) and the effects of relevant variables on various states of the motion of a solid are discussed in the following section.

### 3. Solutions of the Equation of Motion for Steady-Uniform Liquid Flows

The three states of motion of the solid that are considered below include: (1) the threshold conditions, when the motion of the solid is impending; (2) the accelerating motion of the solid, the increase of the velocity of a solid from zero to equilibrium or maximum velocity,  $U_m$ , as it travels downstream; and (3) equilibrium velocity conditions, that is, when the solid has attained the equilibrium velocity.

Before proceeding with the solutions of the equation of motion for the solid, it is instructive to describe the relationships of various flow parameters to each other and to the pipe variables for

steady-uniform liquid flows. The volume rate of flow,  $Q$ , is considered the controlling flow parameter for this study. For a given value of  $Q$  and pipe variables ( $D$ ,  $n$ , and  $S$ ), the value of flow depth ( $h$ ) and water velocity ( $V$ ) can be computed by the use of the Manning equation as [9,10]:

$$Q=(A_w R_w^{2/3} S^{1/2})/n \quad (39)$$

$$V=Q/A_w=(R_w^{2/3} S^{1/2})/n \quad (40)$$

where

$$R_w=(D/4)[1-2(1-2\lambda)(\lambda-\lambda^2)^{1/2}/\cos^{-1}(1-\lambda)] \quad (41)$$

$$\lambda=h/D,$$

and  $A_w$  is given in eq (12).

The momentum flux or specific force,  $M$ , defined in eq (27), may be computed from  $h$  and  $V$ . The flow specific energy may also be computed from  $h$  and  $V$  as:

$$E=h+V^2/2g \quad (42)$$

The quantities  $h$ ,  $V$ ,  $M$ , and  $E$  increase with an increase in  $Q$ . For a given flow rate  $Q$ , quantity  $h$  increases with an increase in  $n$  and decreases with an increase in  $D$  and  $S$ ; the quantities  $V$ ,  $M$ , and  $E$  increase with an increase in  $S$  and decrease with an increase in  $D$  and  $n$ . Variations of  $h$  and  $V$  at a given value of  $Q$ , due to variations in  $D$ ,  $n$ , and  $S$  would affect various terms in the equation of motion of the solid, i.e., eqs (15), (26), or (32).

### 3.1 Threshold Conditions

The minimum value of steady-uniform flow rate required to start the motion of a solid, i.e., threshold flow rate,  $Q_0$ , and other threshold flow parameters may be determined by solving eqs (26) and (32) for the threshold conditions, i.e., when the motion of the solid is impending. At threshold conditions,  $\eta$  represents the coefficient of static friction,  $\eta_s$ , between the solid and the pipe wall in the presence of the liquid. The determination of the value of  $\eta_s$  in the presence of the liquid is complex and considered beyond the scope of this study. Nevertheless,  $\eta_s$  is one of the more important variables because it is the major determining factor of the resistance to the motion of a solid. Also, the quantities  $\alpha$ ,  $C_r$ , and  $U_s$  are all zero at the threshold conditions. For these conditions, eqs (26) and (32) may be rewritten as:

$$V_o^2-2gL(\sigma A_s/A_{swo}-1)[\eta(1-S^2)^{1/2}-S]/(1+A_{swo}/A_{wo})=0 \quad (43)$$

and

$$V_o^2-\{gL(\sigma A_s/A_{swo}-1)[\eta_s(1-S^2)^{1/2}-S]-g\bar{y}(1-A_{swo}/\sigma A_s)\}=0 \quad (44)$$

where  $S=\sin\theta$  =slope of the pipe,

$$A_s=\pi d^2/4,$$

and the other quantities have been previously defined. The free stream liquid velocity  $V_o$ , is

related to the free stream water depth  $h_o$ , through the free stream hydraulic radius  $R_o$ , by the Manning equation as indicated in eq (40).

Substituting for  $V_o$  from eq (40), eqs (43) and (44) may be expressed as:

$$(S^{1/2}R^{2/3}/n)^2 - [gL(\sigma A_s/A_{swo}-1)(\eta_s(1-S^2)^{1/2}-S)](A_{swo}/A_{wo}) = 0 \quad (45)$$

and

$$(S^{1/2}R^{2/3}/n)^2 - [gL(\sigma A_s/A_{swo}-1)[\eta_s(1-S^2)^{1/2}-S] - g\bar{y}(1-A_{swo}/\sigma A_s)] = 0 \quad (46)$$

Since the quantities  $A_{swo}$ ,  $A_{wo}$ ,  $R_o$ , and  $\bar{y}_o$  are all functions of the free stream depth,  $h_o$ , eqs (45) and (46) may be solved by successive iteration to yield a value of  $h_o$  for any values of the variables  $D$ ,  $n$ ,  $S$ ,  $d$ ,  $L$ ,  $\sigma$ , and  $\eta_s$ . This value of the stream depth is the threshold stream depth,  $h_i$ , and the flow rate corresponding to  $h_i$  is the threshold flow rate,  $Q_i$ . Knowing the value of  $h_i$ , quantity  $Q_i$  can be computed by eq (39). The value of threshold flow parameters, i.e.,  $V_i$ ,  $M_i$ , and  $E_i$  may be computed by the use of appropriate equations.

Equations (45), (46), and (39) are applied to examine the effects of the relevant variables on the threshold flow rate in the following section.

### 3.1.1 Effects of the Variables on Threshold Flow Rates

Equations (45) and (39) are applied to examine the effects of the variables on  $Q_i$ . The seven variables under consideration are  $D$ ,  $n$ ,  $S$ ,  $d$ ,  $L$ ,  $\sigma$ , and  $\eta_s$ . The variations of  $Q_i$  due to variations in  $\eta_s$  and another variable, while the remaining five variables are held constant are presented in figures 5-11. An examination of these figures indicates that the value of flow rate,  $Q_i$ , required to initiate the motion of a solid increase with: an increase in the values of  $\eta_s$ ,  $D$ ,  $n$ ,  $d$ ,  $L$ , and  $\sigma$ ; and a decrease in the value of  $S$ . These results also indicate that for a given solid (i.e., fixed values of  $d$ ,  $L$ ,  $\sigma$ , and  $\eta_s$ ) and a given value of  $Q$ , the chance of initiating the motion of the solid can be increased by selecting a pipe with a smaller diameter and with the lower roughness, (i.e., having a

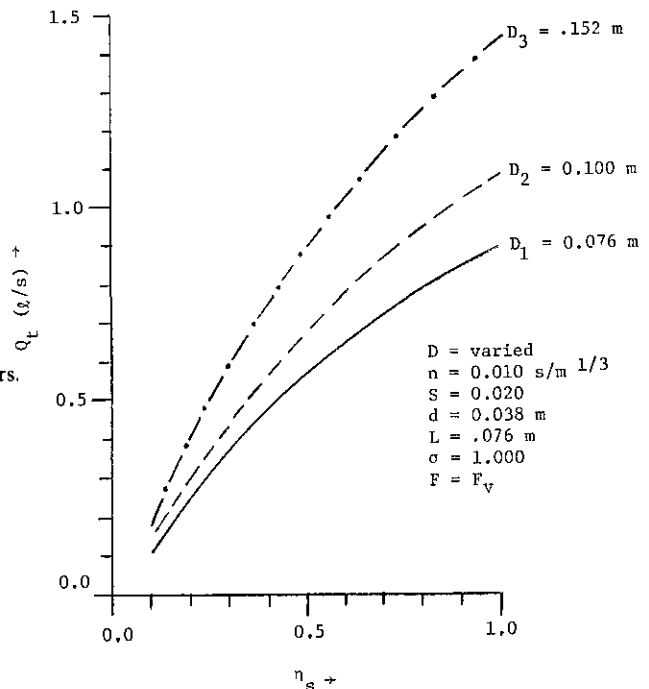


Figure 5— $Q_i$  versus  $\eta_s$  for different values of pipe diameters.

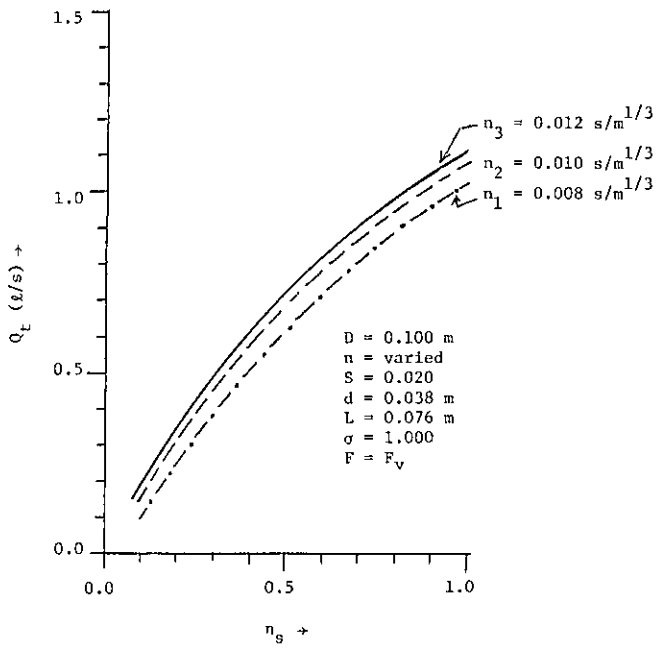


Figure 6— $Q_t$  versus  $\eta_s$  for different values of the Manning coefficient.

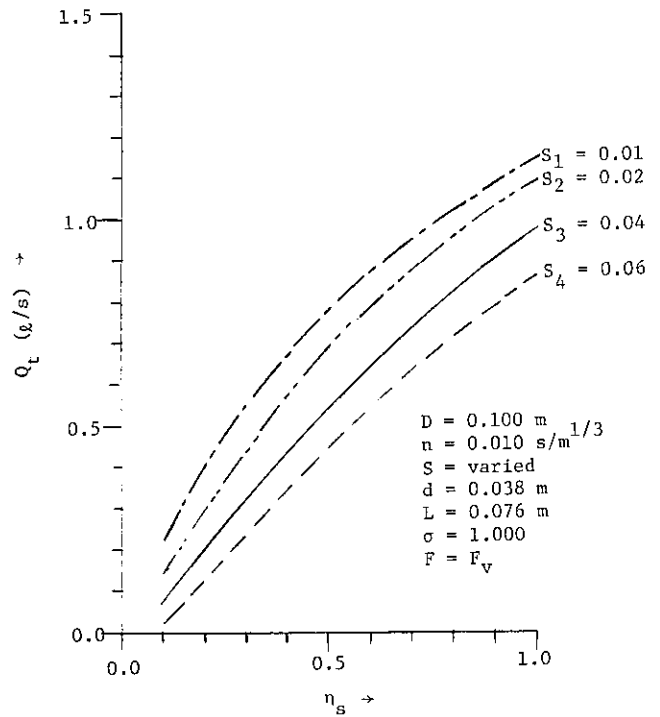


Figure 7— $Q_t$  versus  $\eta_s$  for different values of pipe slope.

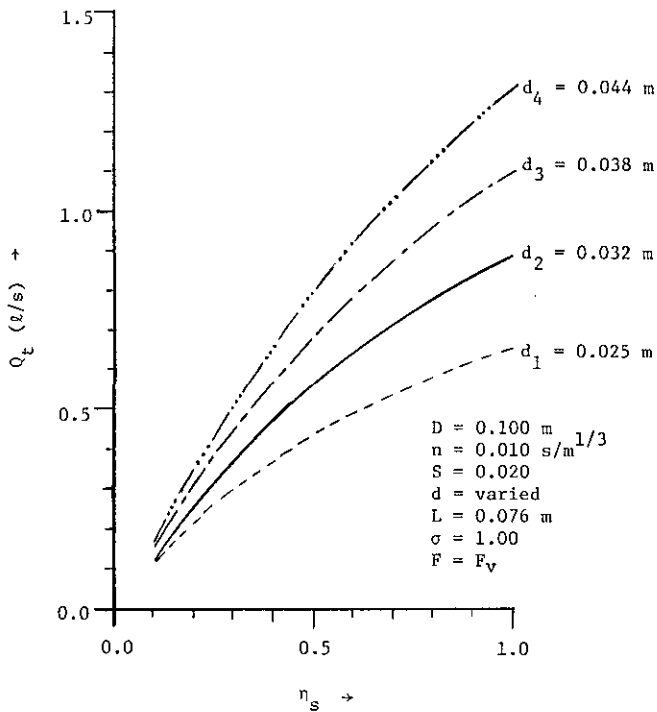


Figure 8— $Q_t$  versus  $\eta_s$  for different values of solid diameter.

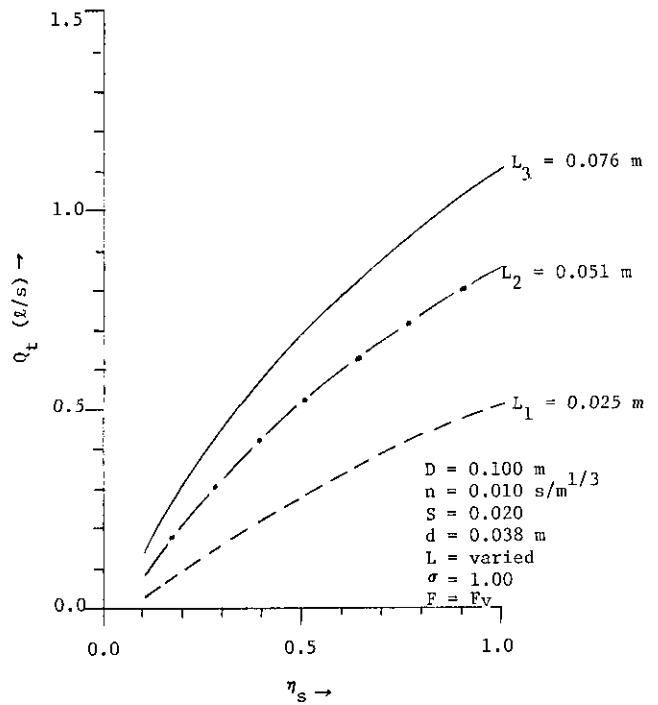


Figure 9— $Q_t$  versus  $\eta_s$  for different values of solid length.

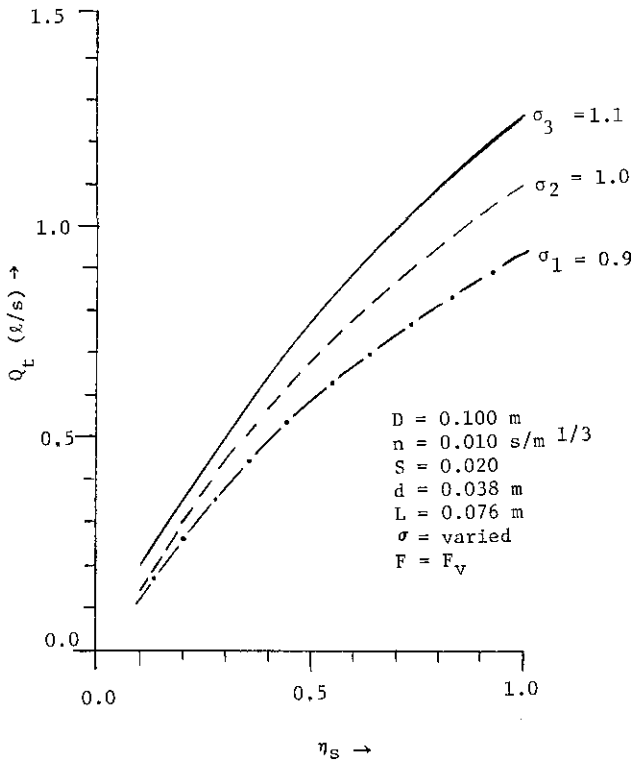


Figure 10— $Q_L$  versus  $\eta_s$  for different values of solid specific gravity.

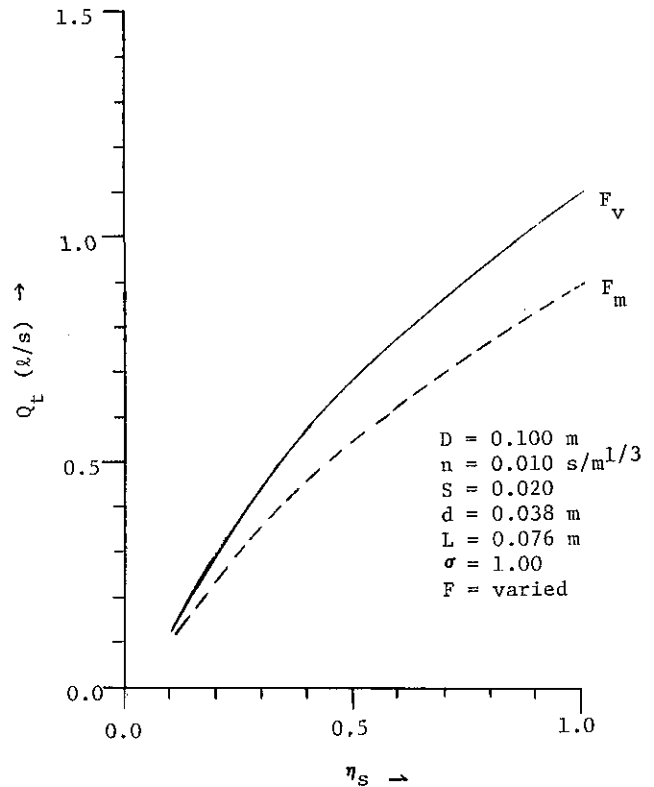


Figure 11— $Q_L$  versus  $\eta_s$  for different force functions.

lower value of the Manning coefficient,  $n$ ), or by increasing the slope or pitch of the pipe.

Equations (45), (46), and (39) are applied to examine the effects on  $Q_L$  of utilizing the two force functions, i.e., the force function  $F_v$  based on the free stream velocity (eq (23)) or the force function  $F_m$  based on the free stream momentum flux (eq (31)). The variations of  $Q_L$  due to variations in  $\eta_s$ , while all other variables are held constant, for the two force functions are shown in figure 11. An examination of this figure indicates that the values of  $Q_L$  obtained by the use of  $F_v$  are larger than those obtained by the use of  $F_m$ . The smaller values of  $Q_L$  resulting from the use of force function  $F_m$  are consistent with the larger magnitude of force  $F_{ws}$  given by  $F_m$  than by  $F_v$  under identical conditions. It suggests that the selection of a proper force function is an important factor in the development of mathematical models for predicting the motion of solids in partially filled pipes.

### 3.2 Accelerating Motion of a Solid

Accelerating motion of a solid, i.e., the increase of the velocity of a solid from zero to  $U_m$ , as it moves downstream in the pipe may be examined by solving eqs (26) and (32). The lift coefficient,  $C_L$ , may be taken as zero without any loss of generality. When the motion of the solid is initiated,  $\eta$  represents the coefficient of kinematic or sliding friction,  $\eta_d$ , between the solid and the pipe wall. Magnitude of  $\eta_d$  is less than that of  $\eta_s$ ; it may vary with the velocity of the solid relative to the pipe wall and it may further decrease if a liquid film is formed between the solid and the pipe wall. However, for the purpose of this study,  $\eta_d$  is considered to be a constant quantity and its value is assumed to be 75% of that of  $\eta_s$ .

Substituting  $C_1$ , equal to zero,  $\rho\sigma LA_s$  for the mass of the solid,  $m$ , and  $dU/dT$  for the acceleration of the solid,  $\alpha$ , into eqs (26) and (32) and rearranging the terms the equations may be rewritten as:

$$(V_o-U)^2-\nu^2=1/N \, dU/dT \quad (47)$$

$$\text{where, } \nu^2=2gL(\sigma A_s/A_{swo}-1)[0.75\eta_s(1-S^2)^{1/2}-S]/(1+A_{swo}/A_{wo}) \quad (48)$$

$$\text{and, } 1/N=2\sigma LA_s/[A_{swo}(1+A_{swo}/A_{wo})] \quad (49)$$

and

$$(V_o-U)^2-\nu_1^2=(1/N_1)dU/dT \quad (50)$$

where

$$\nu_1^2=gL(\sigma A_s/A_{swo}-1)[0.75\eta_s(1-S^2)^{1/2}-S]-g\bar{y}(1-A_{swo}/\sigma A_s) \quad (51)$$

and

$$1/N_1=\sigma LA_s/A_{swo} \quad (52)$$

As indicated earlier, for a given flow rate, the free stream depth and velocity are constant throughout the pipe. Hence, for a given value of  $Q_o$ , and the variables  $D$ ,  $n$ ,  $S$ ,  $d$ ,  $L$ ,  $\sigma$ , and  $\eta_s$ , the quantities  $h_o$ , and  $V_o$  are all constants; and the only quantity in eqs (47) and (50) that varies with time is the velocity of the solid,  $U$ . Equation (47) may be rewritten as:

$$\frac{dU}{(V_o-U)^2-\nu^2} = NdT. \quad (53)$$

The integration of eq (53), for values of  $\nu$  greater than zero and for  $\nu$  equal to zero yields the following:

$$(1/2\nu)\ln\left(\frac{V_o-U+\nu}{V_o-U-\nu}\right)+C_1=NT, \quad \text{for } \nu>0 \quad (54)$$

and

$$1/(V_o-U)+C_2=NT, \quad \text{for } \nu=0 \quad (55)$$

where,  $C_1$  and  $C_2$  are constant, and can be evaluated from the initial condition, i.e., at  $T=0$ ,  $U_o=0$ . For this initial condition eqs (54) and (55) yield,

$$C_1=(1/2\nu) \ln [(V_o+\nu)/(V_o-\nu)],$$

and  $C_2=1/V_o$ .

Substituting for  $C_1$  and  $C_2$  in eqs (54) and (55), respectively, and rearranging terms, these equations may be rewritten for  $U_s$  as:

$$U=V_o-\nu \left(\frac{1+Be^{-bT}}{1-Be^{-bT}}\right) = \frac{(V_o^2-\nu^2) \tanh(bT/2)}{(\nu+V_o) \tanh(bT/2)}, \quad \text{for } \nu>0 \quad (56)$$

and

$$U = V_o^2 NT / (1 + V_o NT), \quad \text{for } \nu = 0 \quad (57)$$

where,  $B = (V_o - \nu) / (V_o + \nu)$

and  $b = 2 \nu N$ .

Equations (56) and (57) give variations of  $U$  with time. These equations indicate that the value of maximum velocity attained by a solid is equal to  $V_o - \nu$  when  $\nu$  is greater than zero and  $V_o$  when  $\nu$  is equal to zero.

Equation (56) indicates that  $U$  will be equal to  $U_m$  at a time,  $T$ , for which  $\tanh(bT/2)$  is unity or when  $bT/2$  is equal to or greater than 6.5. Equation (57) indicates that  $U$  will be equal to  $U_m$  at a time,  $T$ , equal to infinity. Or

$$U_m = V_o - \nu \text{ at } T = 6.5 / \nu N, \quad \text{for } \nu > 0 \quad (58)$$

$$U_m = V_o, \text{ at } T = \infty, \quad \text{for } \nu = 0. \quad (59)$$

Since  $U = dX_s / dT$ , eqs (56) and (57) may be integrated to determine the distance,  $X_s$ , traversed by a solid. Initially, at time  $T$ , equal to zero,  $X_s$  is zero, for this initial condition integration of eqs (56) and (57) yields the following expressions for  $X_s$ ,

$$X_s = (V_o - \nu)T - (1/N) \ln \left( \frac{1 - Be^{-bT}}{1 - B} \right), \quad \text{for } \nu > 0 \quad (60)$$

and

$$X_s = V_o T - (1/N) \ln(1 + V_o NT), \quad \text{for } \nu = 0. \quad (61)$$

Equations (60) and (61) give the variation of  $X_s$  with time. Equations (56) and (60) may be applied simultaneously to study the variations of  $U$  with the axial distance or as the solid travels downstream from its starting position for  $\nu$  greater than zero. And for values of  $\nu$  equal to zero, eqs (57) and (61) may be applied simultaneously to examine the variations of  $U$  as the solid travels downstream. Solutions of eq (50), i.e., the expressions for  $U$  and  $X_s$  corresponding to the force function  $F_m$  may be obtained by replacing  $N$  and  $\nu$  by  $N_1$  and  $\nu_1$  in eqs (56) to (61). The effects of the variables on the accelerating motion of a solid are examined below.

### 3.2.1 Effects of the Variables on the Accelerating Motion of a Solid

Equations (56) through (61) are applied to examine the effects of  $Q$  and the variables  $D$ ,  $n$ ,  $S$ ,  $d$ ,  $L$ ,  $\sigma$ , and  $\eta_s$  on the accelerating motion of the solid. The velocity-histories of a solid, that is, the increase with time of the nondimensional velocity,  $U/U_m$ , of a solid from 0.0 to 0.99, are shown in figures 12–20. Each figure shows the effects of one variable on the velocity-history. An examination of these figures indicates the following: (1) the flow rate  $Q$  and the variables  $D$ ,  $n$ ,  $S$ , and  $\sigma$  do not have a significant effect on the velocity-history of a solid; (2) the variables  $d$ ,  $L$ , and  $\eta_s$  do affect the velocity-history, and the time required for  $U$  to be equal to  $U_m$  increases with an increase in  $d$ ,  $L$ , and  $\eta_s$ ; and (3) the velocity-history is not significantly affected by the force function (fig. 20).

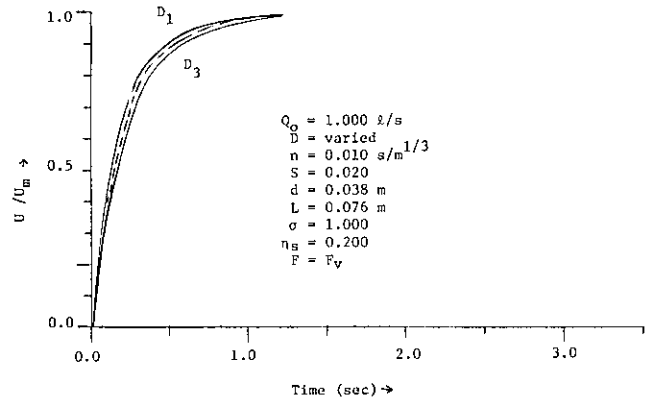
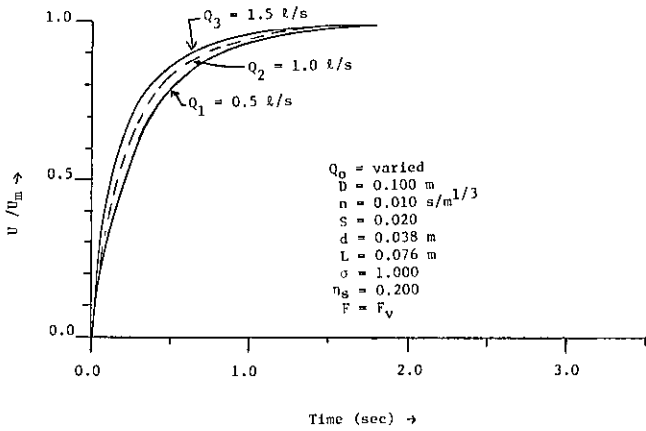


Figure 12—Nondimensional solid velocity,  $U/U_m$ , versus time, for different values of flow rate.

Figure 13—Nondimensional solid velocity,  $U/U_m$ , versus time, for different values of pipe diameter.

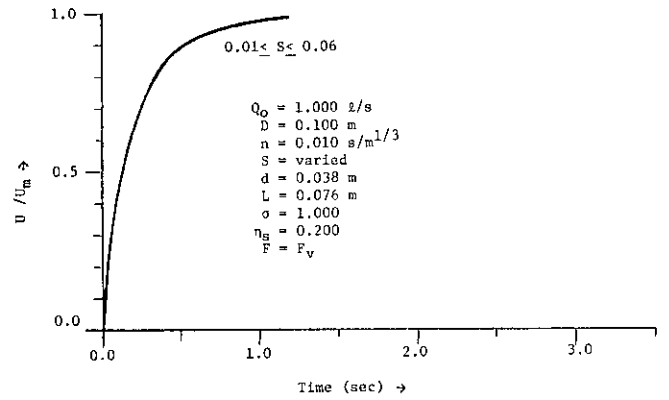
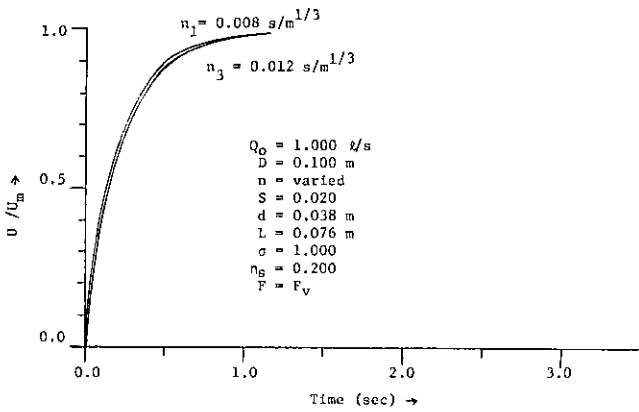


Figure 14—Nondimensional solid velocity,  $U/U_m$ , versus time, for different values of Manning coefficient.

Figure 15—Nondimensional solid velocity,  $U/U_m$ , versus time, for different values of pipe slope.

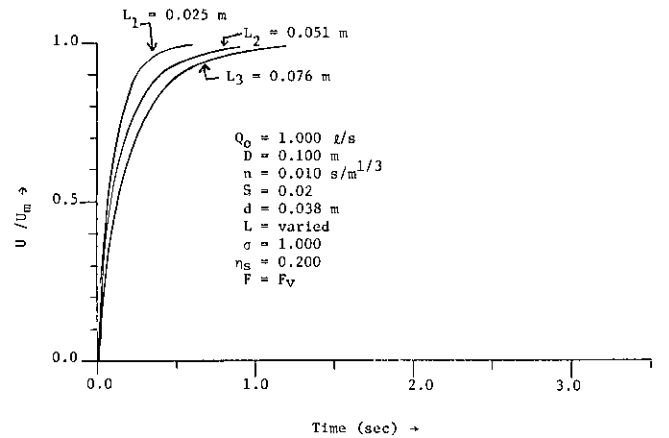
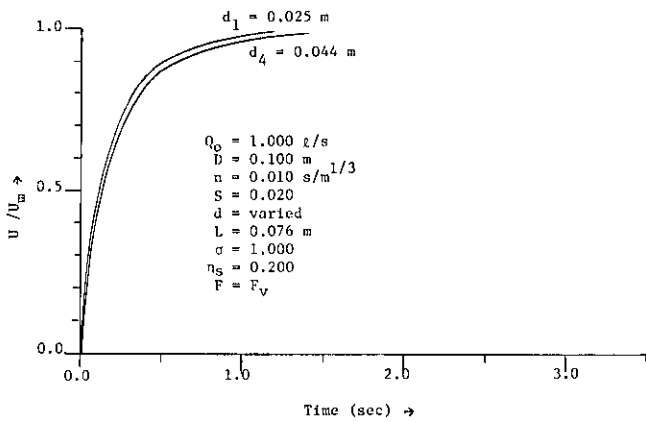
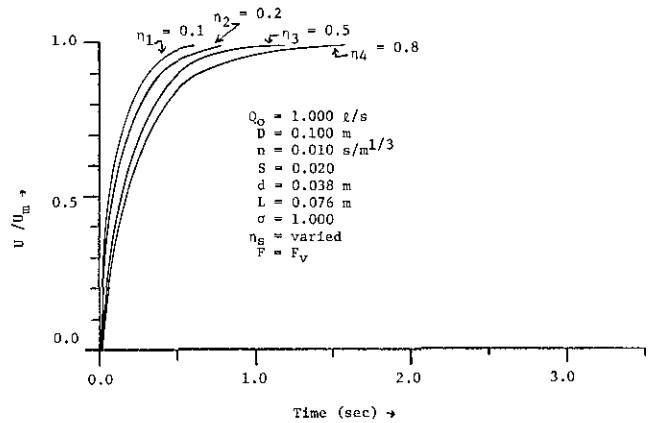
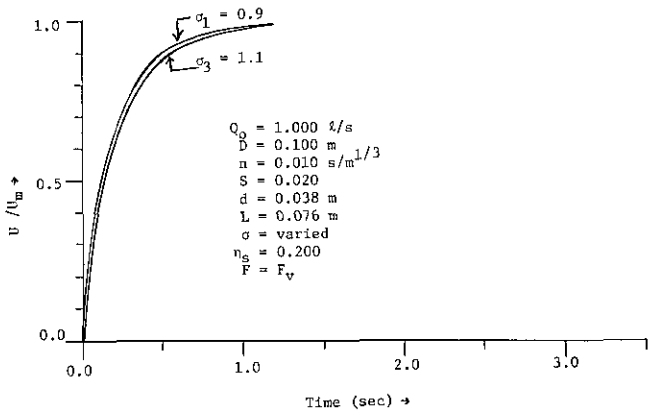


Figure 16—Nondimensional solid velocity,  $U/U_m$ , versus time, for different values of solid diameter.

Figure 17—Nondimensional solid velocity,  $U/U_m$ , versus time, for different values of solid length.

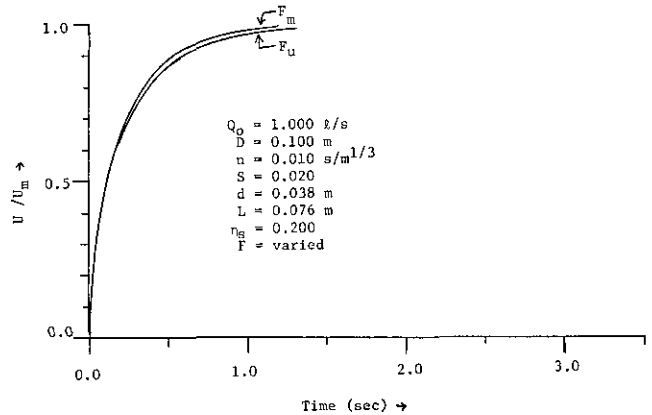


(Clockwise from above)

Figure 18—Nondimensional solid velocity,  $U/U_m$ , versus time, for different values of solid specific gravity.

Figure 19—Nondimensional solid velocity,  $U/U_m$ , versus time, for different values of  $\eta_s$ .

Figure 20—Nondimensional solid velocity,  $U/U_m$ , versus time, for different force functions.

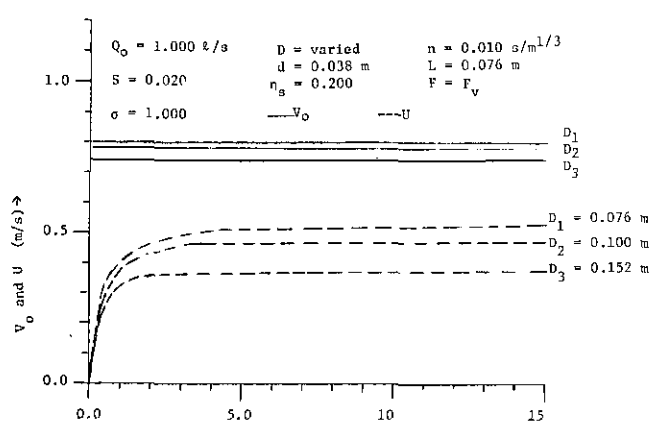
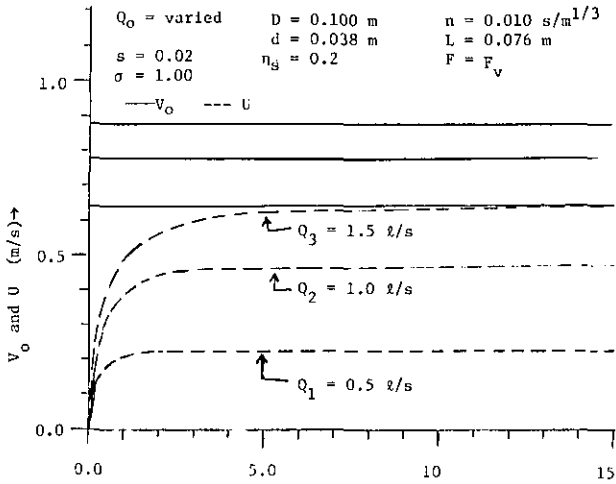


The velocity-distance profiles of a solid, that is, the variation of the velocity of a solid with the nondimensional axial distance,  $X/D$ , traversed by the solid are shown in figures 21–29. Each of these figures shows the effect of one of the variables ( $Q$ ,  $D$ ,  $n$ ,  $S$ ,  $d$ ,  $L$ ,  $\sigma$ ,  $\eta_s$ , and  $F_v$  or  $F_m$ ) on the velocity-distance profile of a solid. An examination of these figures indicates the following: (1) the distance traversed by a solid during its acceleration from rest to a velocity of  $0.99 U_m$  increases with an increase in  $Q$ ,  $S$ , and  $L$ , and decreases with an increase in  $D$ ,  $n$ ,  $d$ ,  $\sigma$ , and  $\eta_s$ ; (2) the velocity,  $U$ , of a solid at a given axial distance increases with an increase in  $Q$  and  $S$ ; (3) the value of  $U$  at a given axial distance decreases with an increase in  $D$ ,  $n$ ,  $d$ ,  $L$ ,  $\sigma$ , and  $\eta_s$ ; and (4) the velocities of a solid at all axial distances are higher when  $F_m$  is used than when  $F_v$  is used.

### 3.3 Equilibrium Velocity Conditions

The equilibrium velocity of a solid, for steady-uniform flow is a constant quantity, and it is the maximum velocity that a solid can attain for a given value of flow rate. The expression for the equilibrium or maximum velocity,  $U_m$ , is given in eq (58) for  $\nu > 0$ , and in eq (59) for  $\nu = 0$ . The expression for  $U_m$  may also be obtained by letting  $dU/dT$  equal to zero in eqs (47) and (50), and are:

$$U_m = V_o - \nu, \text{ for force function } F_v, \quad (63)$$



(Clockwise from above)

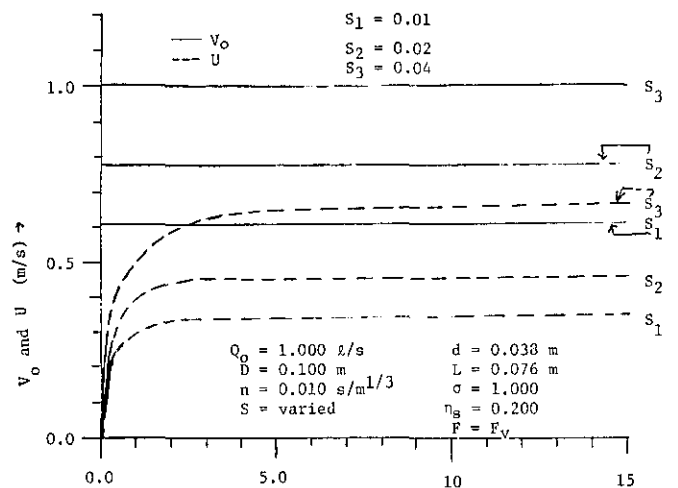
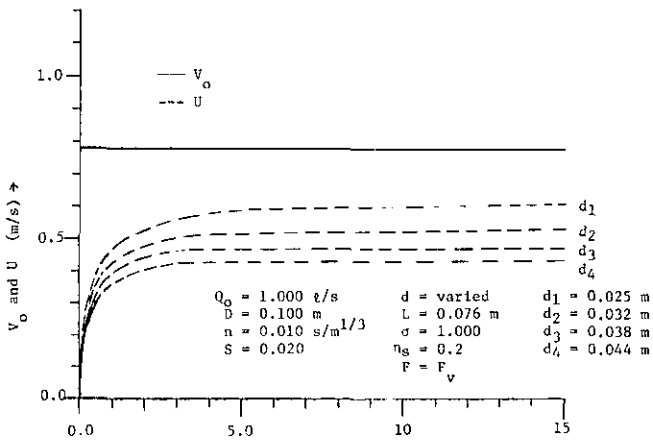
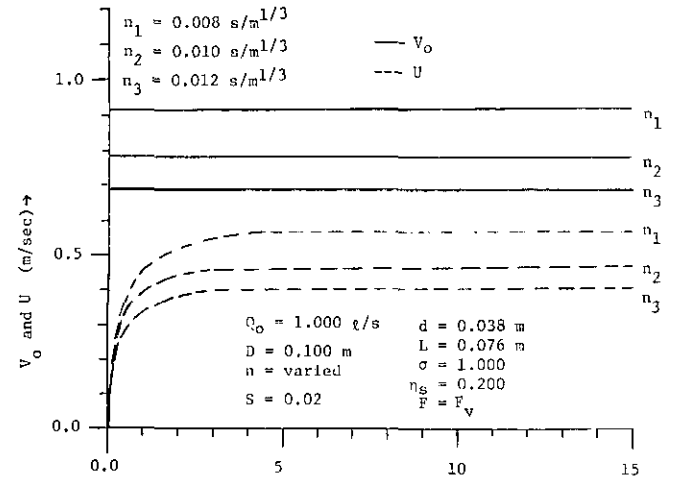
**Figure 21**—Solid velocity versus nondimensional axial distance, for different values of flow rate.

**Figure 22**—Solid velocity versus nondimensional axial distance, for different values of pipe diameter.

**Figure 23**—Solid velocity versus nondimensional axial distance, for different values of Manning coefficient.

**Figure 24**—Solid velocity versus nondimensional axial distance, for different values of pipe slope.

**Figure 25**—Solid velocity versus nondimensional axial distance, for different values of solid diameter.



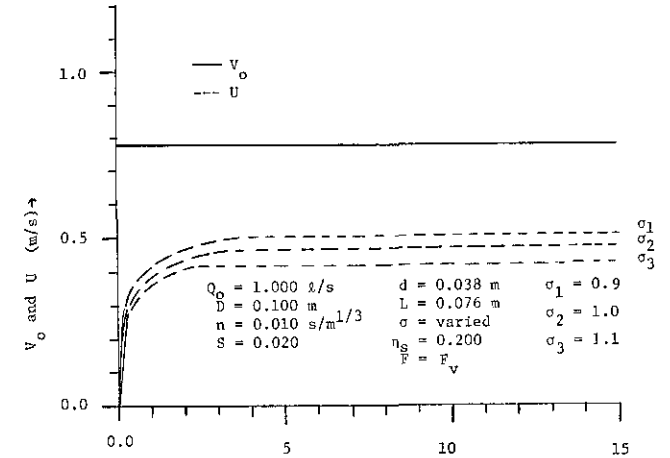
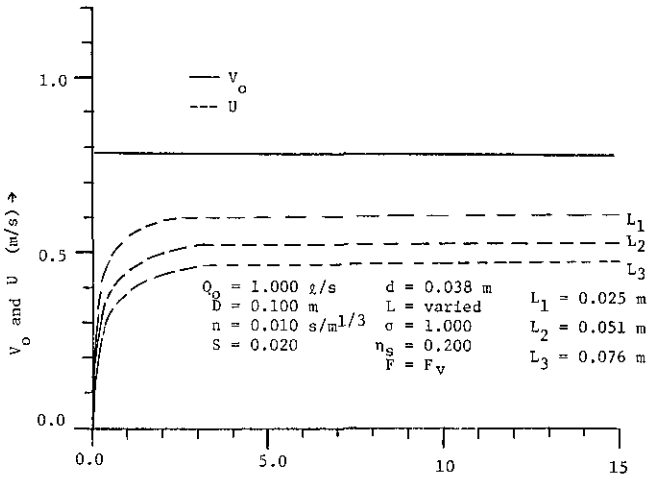


Figure 26—Solid velocity versus nondimensional axial distance, for different values of solid length.

Figure 27—Solid velocity versus nondimensional axial distance, for different values of solid specific gravity.

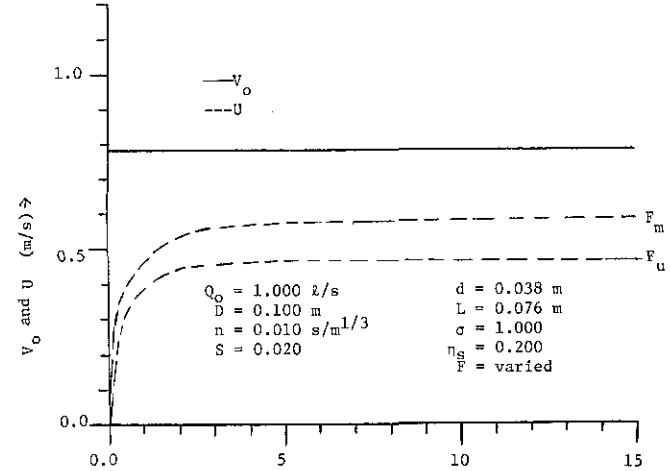
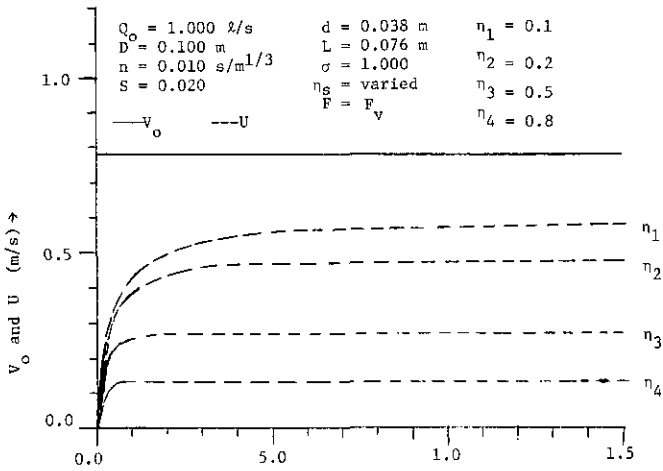


Figure 28—Solid velocity versus nondimensional axial distance, for different values of  $\eta_c$ .

Figure 29—Solid velocity versus nondimensional axial distance, for different force functions.

and

$$U_m = V_o - v_1, \text{ for force function } F_m, \quad (64)$$

where,  $v$  and  $v_1$  are given in eqs (49) and (52), respectively.

The effects of the variations of flow rate  $Q$  and various variables  $U_m$  are examined below.

### 3.3.1 Effects of the Variables on the Maximum Velocity of a Solid

Equations (39), (44), and (63) are applied to examine the effects of the liquid flow rate,  $Q$ , and of the variables  $D$ ,  $n$ ,  $S$ ,  $d$ ,  $L$ ,  $\sigma$ , and  $\eta_s$  on  $U_m$ . The variations of  $U_m$  due to variations of  $Q$  and one variable, while the other six variables are held constant, are shown in figures 30–37. The

corresponding variations of  $V_o$  are also shown in these figures for comparison. The maximum value of  $Q$  considered for this study is equal to 2.0 l/s (or about 31.4 gal/min); this value of  $Q$  corresponds to the approximate value of the peak water flow rate from water closets. An examination of these figures indicates the following: (1) both  $V_o$  and  $U_m$  increase with an increase in  $Q$ ; (2) as indicated earlier, flow velocity,  $V_o$ , increases with an increase in  $S$  and a decrease in  $D$  and  $n$ ; and (3) the maximum velocity of solid,  $U_m$ , increases with an increase in  $S$ , and it decreases with an increase in  $D$ ,  $n$ ,  $d$ ,  $L$ ,  $\sigma$ , and  $\eta_s$ .

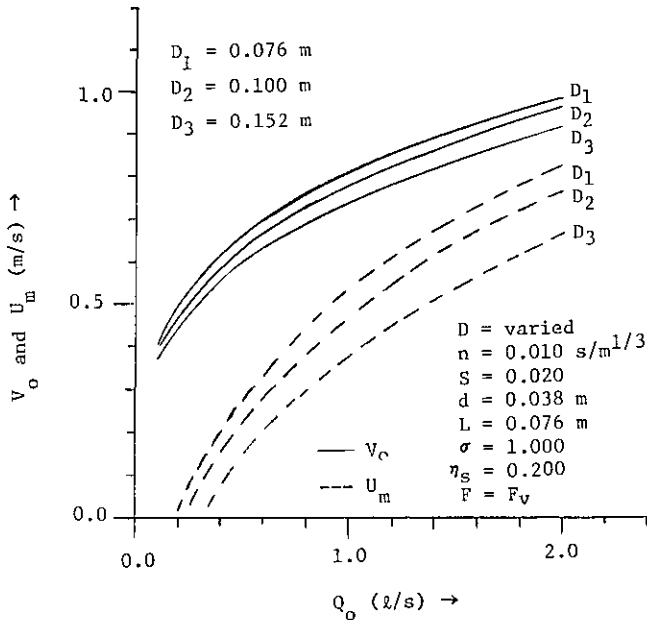


Figure 30-The maximum velocity,  $U_m$ , of a solid versus  $Q_o$ , for different values of pipe diameter.

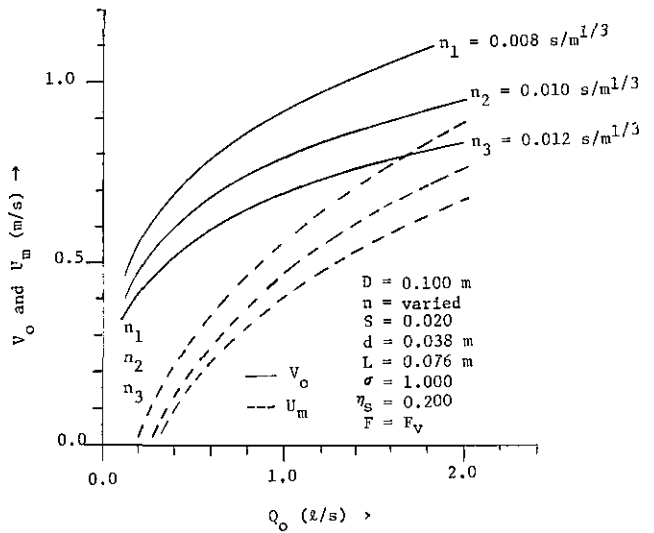


Figure 31. The maximum velocity,  $U_m$ , of a solid versus  $Q_o$  for different values of pipe diameter

Figure 31-The maximum velocity,  $U_m$ , of a solid versus  $Q_o$ , for different values of Manning coefficient.

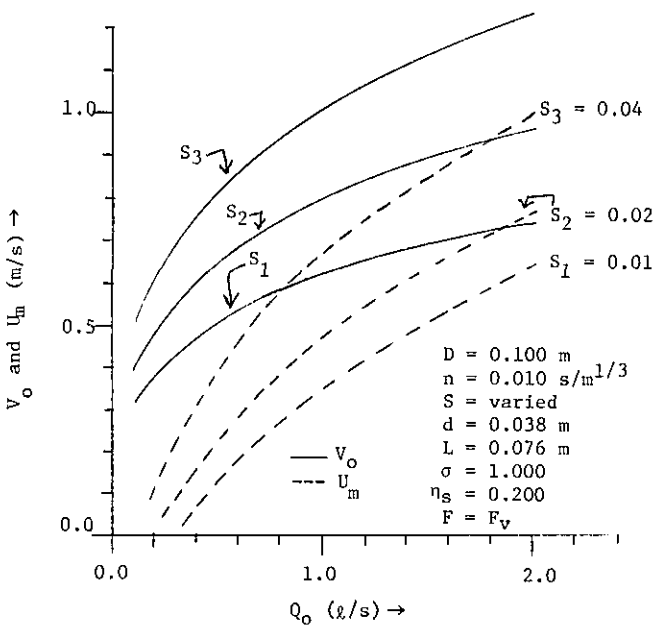


Figure 32-The maximum velocity,  $U_m$ , of a solid versus  $Q_o$ , for different values of pipe slope.

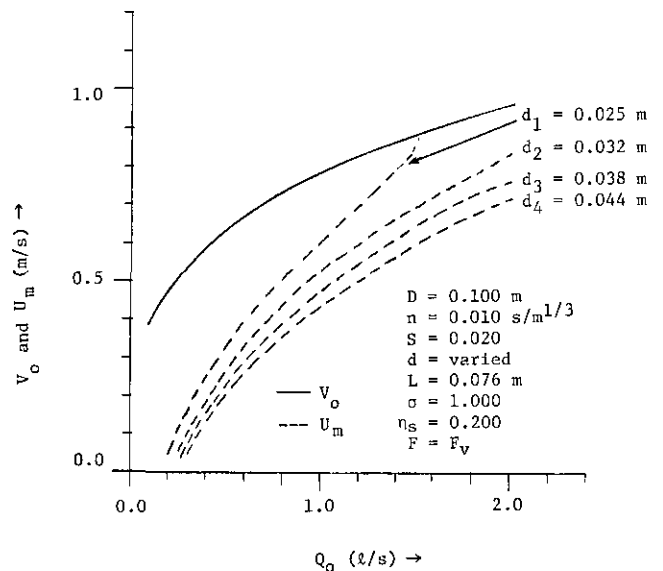


Figure 33-The maximum velocity,  $U_m$ , of a solid versus  $Q_o$ , for different values of solid diameter.

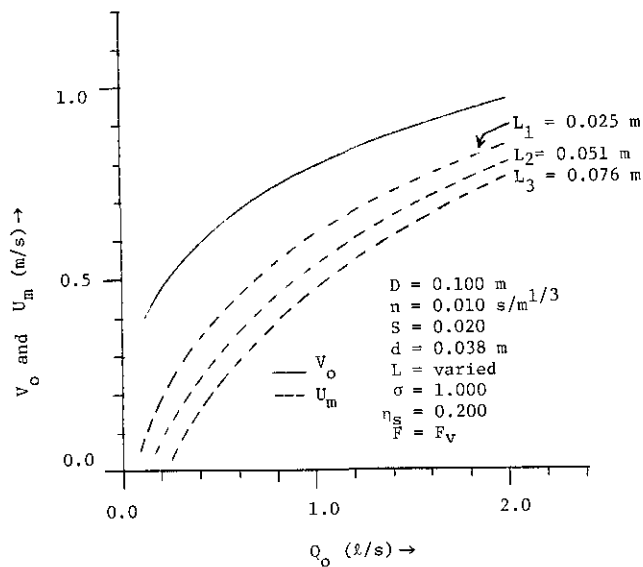


Figure 34—The maximum velocity,  $U_m$ , of a solid versus  $Q_o$ , for different values of solid length.

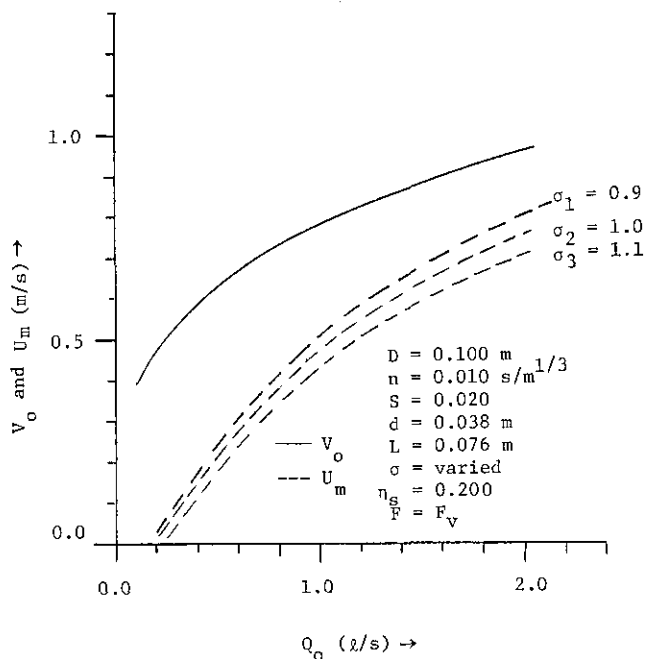


Figure 35—The maximum velocity,  $U_m$ , of a solid versus  $Q_o$ , for different values of solid specific gravity.

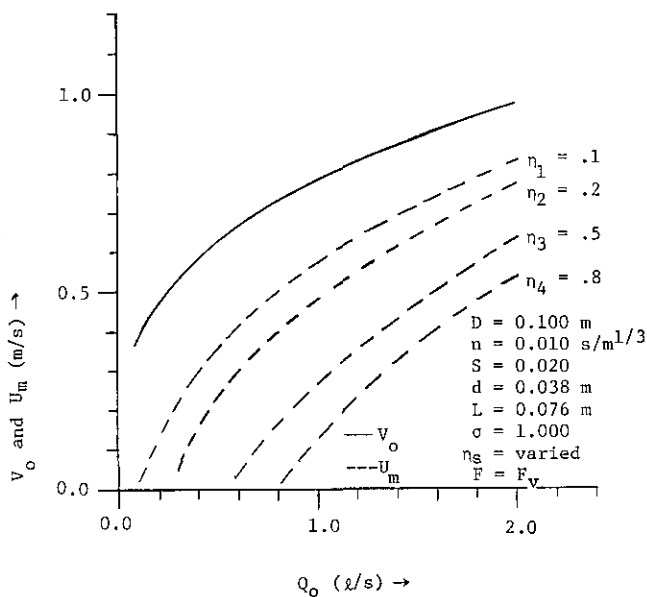


Figure 36—The maximum velocity,  $U_m$ , of a solid versus  $Q_o$ , for different values of  $\eta_s$ .

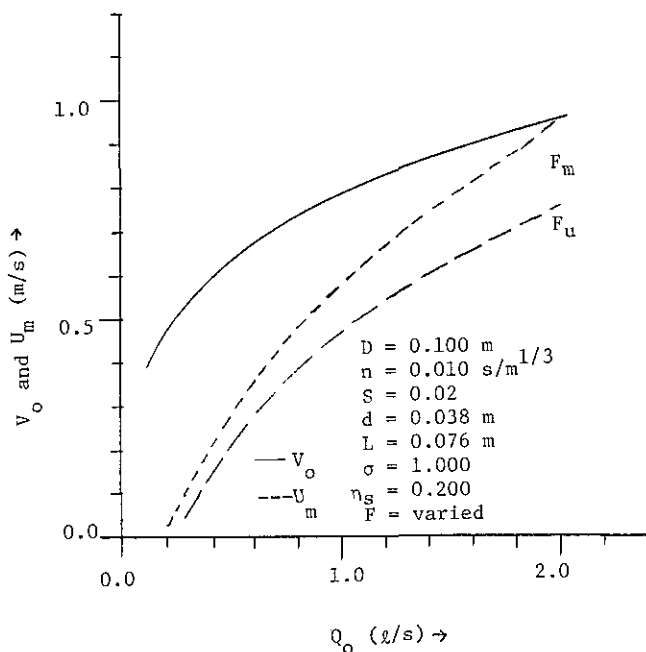


Figure 37—The maximum velocity,  $U_m$ , of a solid versus  $Q_o$ , for different force functions.

Equations (63) and (64) are applied to examine the effects of the two force functions on  $U_m$ . The variations of  $U_m$  due to variations of  $Q$ , for a set of values of the variables are shown in figure 37. An examination of this figure indicates the values of  $U_m$  are higher for  $F_m$  than those for  $F_v$ . The larger values of  $U_m$  attained by a solid when force function  $F_m$  is used, are consistent with the larger magnitude of force given by  $F_m$  than by  $F_v$  under identical conditions.

### 3.4 Comparison with Experimental Data

An experimental study of the motion of single solids with steady uniform flows in partially filled pipes was carried out under the sponsorship of NBS at Brunel University, U.K. [16]. In this study, the solid was introduced into the established flow with some initial velocity via a 50 mm tube and a 45° elbow and the effects of some variables ( $Q$ ,  $S$ ,  $L$ ,  $d$ , and  $\sigma$ ) on the velocity of the solid ( $U$ ) were examined. The details of the experimental equipment and procedures may be found in reference [16]. Examples of typical data from reference [16] are reproduced in figures 38 and 39.

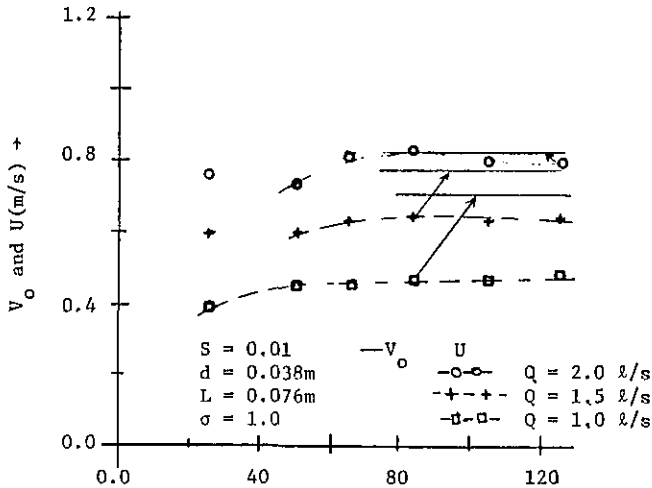


Figure 38—Solid velocity measured along the 100 mm diameter pipe compared with the free stream water velocity (Ref. 16).

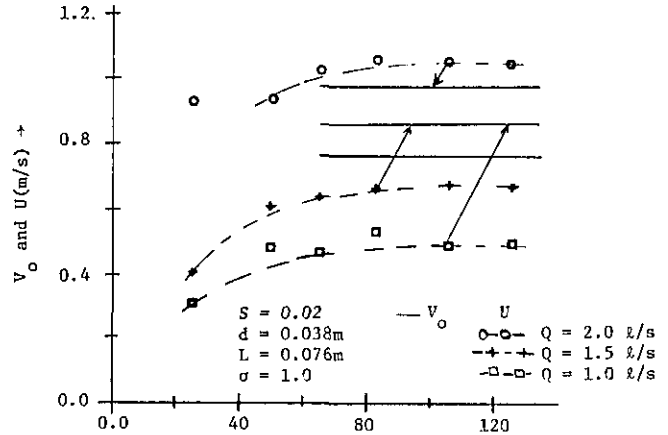


Figure 39—Solid velocity measured along the 100 mm diameter pipe compared with the free stream water velocity (Ref. 16).

The experimental data indicate that the effects of the variables ( $Q$ ,  $S$ ,  $L$ ,  $d$ , and  $\sigma$ ) on the solid velocity predicted by the analysis (figs. 21–29) are qualitatively consistent with the data of reference [16]. The observed values of the maximum solid velocity are fairly close to the results predicted by eqs (56) through (59) for the magnitude of  $\eta_s$  equal to about 0.1, except for the experiments with a flow rate of 2 l/s. The data for the flow rates of 2 l/s indicate that the solid velocity ( $U$ ) is somewhat higher than the free stream velocity ( $V_o$ ) of the carrier liquid calculated from the measured values of flow depth. These results may be explained as follows.

When the quantity  $W_b(1-C_f)$  is equal to zero, then the solid no longer drags on the pipe wall but moves as a waterborne object situated in the flow somewhere above and away from the pipe wall. The free stream velocity ( $V_o$ ), calculated by the Manning equation or by the measured flow depth, represents the average value of the flow velocity averaged over the wetted portion of the cross-section area. Considering the velocity distribution of a partially filled pipe flow at a pipe cross-section, the value of average velocity,  $V_o$  may be somewhat less than the velocity of the liquid adjacent to the waterborne solid moving with velocity,  $U$ . However, the available data are too few to draw any definite conclusions.

Equations (56) through (59) are not capable of predicting this phenomenon. Since the analysis leading to these equations has been based on free stream conditions derived from the Manning equation, it limits the maximum value of  $U$  to  $V_o$ .

Typical data showing the velocity of single solids induced by surge flows in a partially filled pipe are reproduced from reference [4] in figures 40 and 41. The effects of the variables ( $D$ ,  $S$ ,  $L$ ,

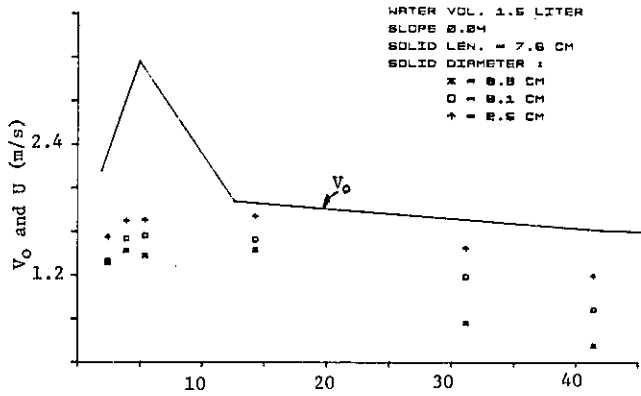


Figure 40—Solid velocity versus nondimensional axial distance for 7.6 cm long solids and for water volume=1.5 L, and  $S=0.04$  (Ref. 4).

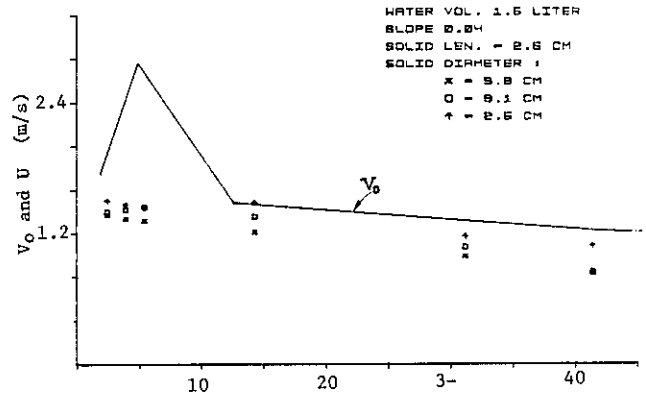


Figure 41—Solid velocity versus nondimensional axial distance for 2.5 cm long solids and for water volume=1.5 L, and  $S=0.04$  (Ref. 4).

$d$ , and  $\eta_s$ ), predicted by the analysis for steady uniform flow are also qualitatively consistent with the data of references [3] and [4].

The qualitative consistency between the predicted and observed effects of variables on the flow-induced velocity of a solid confirms the form of the analysis presented. The available experimental data also illustrate the limitations of the model inherent in the use of free stream velocity derived from a one-dimensional representation of flow such as the Manning equation.

#### 4. Conclusions

A general equation for the liquid flow-induced motion of a solid is developed. Two alternate force models, one based on free stream velocity and the other on free stream momentum flux, are formulated to approximate the flow-induced force acting on the solid. These force models simplify the equation of motion. The simplified equation is solved for steady uniform liquid flows to examine the effects of flow rate ( $Q$ ), pipe variables ( $D$ ,  $n$ , and  $S$ ), solid variables ( $d$ ,  $L$ , and  $\sigma$ ), coefficient of friction between solid and pipe wall ( $\eta_s$ ), and the force functions ( $F_v$  or  $F_m$ ) on the motion of the solid.

The minimum value of flow rate required to initiate the motion of a solid, or the threshold flow rate, increases with an increase in  $D$ ,  $n$ ,  $d$ ,  $L$ ,  $\sigma$ , and  $\eta_s$  and decreases with an increase in  $S$ . The flow rates required to initiate the motion of solid predicted by the use of  $F_v$  are larger than those predicted by the use of  $F_m$ .

The maximum velocity attained by a solid as well as the velocity of the solid at a given axial distance of the pipe increase with an increase in  $Q_o$  and  $S$ , and decrease with an increase in  $D$ ,  $n$ ,  $d$ ,  $L$ ,  $\sigma$ , and  $\eta_s$ . The qualitative effects of the variables  $Q_o$ ,  $D$ ,  $S$ ,  $d$ ,  $L$ , and  $\eta_s$  on the velocities of the solids are consistent with the available experimental data. The velocities of a solid predicted by the use of  $F_v$  are lower than those predicted by  $F_m$ .

The qualitative consistency between the predicted and observed effects of the different variables on the motion of the solid demonstrates the validity of the analysis presented. To obtain quantitative agreement between the predicted and experimental results, and to determine which of the two force models is better suited for the problem it is necessary to determine or assume the values of the coefficient of friction between a solid and the pipe wall in the presence of the liquid.

## References

- [1] Yalin, M. S. *Mechanics of sediment transport*. New York: Pergamon Press; 1972.
- [2] Govior, A. W.; Azia, K. *The flow of complex mixtures in pipes*. New York: Van Nostrand Reinhold Company; 1972.
- [3] Mahajan, Bal M. Experimental investigation of transport of finite solids in a 76 mm-diameter partially-filled pipe. Natl. Bur. Stand. (U.S.) NBSIR 81-2266; 1981 April.
- [4] Mahajan, Bal M. Experimental investigation of transport of discrete solids with surge flows in a 10.0 cm diameter partially-filled pipe. Natl. Bur. Stand. (U.S.) NBSIR 81-2450; 1982 January.
- [5] Karnata, M., et al. Studies on flow and transport of feces in horizontal waste pipes. Proc. of the CIB W62 Seminar on Drainage and Water Supply in Buildings, Paris, France; 1979 November.
- [6] Swaffield, J. A.; Marriott, B. S. T. An investigation of the effects of reduced volume W. C. flush on the transport of solids in above ground drainage systems. Proc. of CIB W62 Symposium, Brussels, Belgium; 1978 May.
- [7] Swaffield, J. A.; Wakelin, R. H. M. A study of the interaction of drainage system loading and reduced flush W. C. operation. Proc. of the CIB W62 Seminar on Drainage and Water Supply in Buildings, Paris, France; 1979 November.
- [8] Swaffield, J. A. Application of the method of characteristics to model the transport of discrete solids in partially filled pipe flow. Natl. Bur. Stand. (U.S.) Bldg. Sci. Ser. 139; 1982 February.
- [9] Chow, V. T. *Open-channel hydraulics*. New York: McGraw-Hill Book Company; 1959.
- [10] Henderson, F. M. *Open channel flow*. New York: The MacMillan Company; 1967.
- [11] Ackers, P.; Harrison, J. M. Attenuation of flood waves in part-full pipes. Proc. I.C.E. (London), Vol. 28; 1964 July.
- [12] Price, R. K. Comparison of four numerical methods for flood routing. HY7—July 74: 879: 10659.
- [13] Swaffield, J. A. An initial study of the application of the numerical method of characteristics to unsteady flow analysis in partially filled gravity drainage sized pipes. Natl. Bur. Stand. (U.S.) NBSIR 81-2308; 1981 July.
- [14] Rouse, H. *Elementary mechanics of fluids*. New York: John Wiley and Sons, Inc.; 1964.
- [15] John, J. E. A.; Haberman, W. *Introduction to fluid mechanics*. Englewood, N.J.: Prentice-Hall, Inc.; 1971.
- [16] Swaffield, J. A.; Bridge, S.; Galowin, L. S. Mathematical modeling of time dependent wave attenuation and discrete solid body transport in gravity driven partially filled pipe flows. Brunel University Report No. DREG/NBS/6, 1982 January.